International Journal of Earth Sciences
https://doi.org/10.1007/s00531-024-02410-0

ORIGINAL PAPER

Transtension or transpression? Tectono-metamorphic constraints on the formation of the Monte Grighini dome (Sardinia, Italy) and implications for the Southern European Variscan belt

A. Petroccia[1] · R. Carosi[1] · C. Montomoli[1] · S. Iaccarino[1] · J. B. Forshaw[2] · M. Petrelli[3]

Received: 2 February 2023 / Accepted: 29 March 2024

Abstract
This work presents an integrated structural, kinematic, and petrochronological study of the Monte Grighini dome within the Variscan hinterland–foreland transition zone of Sardinia (Italy). The area is characterised by dextral transpressive deformation partitioned into low- and high-strain zones (Monte Grighini shear zone, MGSZ). Geothermobarometry of one sample of sillimanite-bearing mylonitic metapelite indicates that the Monte Grighini shear zone developed under high-temperature (~ 625 °C) and low-pressure (~ 0.4–0.6 GPa) conditions. In situ U–(Th)–Pb monazite geochronology reveals that the deformation in the shear zone initiated at ca. 315 Ma. Although previous studies have interpreted the Monte Grighini shear zone to have formed in a transtensional regime, our structural and kinematic results integrated with constraints on the relative timing of deformation indicate that it shows similarities with other dextral ductile transpressive shear zones in the Southern European Variscan belt (i.e., the East Variscan Shear Zone, EVSZ). However, dextral transpression in the Monte Grighini shear zone started later than in other portions of the EVSZ within the framework of the Southern European Variscan Belt due to the progressive migration and rejuvenation of deformation from the core to the external sectors of the belt.

Keywords Shear zone · Sardinian Variscan belt · Mylonites · Vorticity · East Variscan Shear Zone · Petrochronology

Introduction

Dome-shaped structures, characterised by a core of high-grade metamorphic or granitic rocks surrounded by low-grade rocks, are important tectonic features in orogens (Burg et al. 2004; Whitney et al. 2004, 2013; Platt et al. 2015; Cao et al. 2022). Their origin and tectonic setting are still debated, and several mechanisms have been proposed for their formation, tectonic regime, and exhumation (Coney et al. 1980; Whitney et al. 2004). During the 1980s and 1990s, these dome-shaped structures were interpreted as metamorphic core complexes (MCCs; Coney et al. 1980; Coney and Harms 1984; Lister and Davis 1989) as inferred in the Basin and Range province (western North America). The formation of MCCs has been attributed to both extensional and compressional tectonic regimes (e.g., Searle and Lamont 2020; Cao et al. 2022). Recent studies have highlighted the importance of strike-slip movement, i.e., transcurrent, transtensional or transpressional tectonics all as a general concept for exhumation processes (e.g., Nabavi et al. 2020) and in the formation of dome-shaped structures (Druguet 2001; Denèle et al. 2007, 2009; Gébelin et al. 2009; Zhang et al. 2017). Transtension or transpression involves km-scale, high-temperature (HT) ductile shear zones, which contribute to the exhumation and the possible emplacement of igneous intrusions (Druguet 2001; Rosenberg and Handy 2005). For this reason, a multidisciplinary approach combining structural investigations with petrochronology is required to better constrain the formation of dome-shaped structures (e.g., Aguilar et al. 2015; Broussolle et al. 2015; Zhang et al. 2017; Cao et al. 2022; Chen et al. 2022; Fu et al. 2022; Spencer et al. 2022).

The Variscan orogeny in Europe comprises numerous dome-shaped structures that developed between the collisional stage at ca. 360–350 Ma and the collapse of the

✉ C. Montomoli
chiara.montomoli@unito.it

1 Earth Science Department, University of Turin, Turin, Italy

2 Institute of Geological Sciences, University of Bern, Bern, Switzerland

3 Dipartimento di Fisica e Geologia, Università degli Studi di Perugia, Perugia, Italy

Published online: 30 April 2024

orogen at ca. 300–290 Ma (Vanderhaeghe and Teyssier 2001; Faure et al. 2009; Gapais et al. 2015; Cochelin et al. 2021; Vanderhaeghe et al. 2020; Vanardois et al. 2022a, b). The development of the Variscan chain was also widely affected by the activity of crustal-scale strike-slip shear zones during the late-Carboniferous ca. 340–300 Ma (Arthaud and Matte 1977; Matte 2001; Carosi and Palmeri 2002; Di Vincenzo et al. 2004; Carreras and Druguet 2014; Franke et al. 2017; Simonetti 2021; Schulmann et al. 2022; Franke and Żelaźniewicz 2023).

The Monte Grighini dome, exposed in the Variscan belt in central Sardinia, is a NW–SE elongated dome within the Nappe Zone (Musumeci 1992). Elter et al. (1990) interpreted the Monte Grighini dome to have resulted from late-Carboniferous strike-slip movement in a shear zone. In contrast, Cruciani et al. (2016) interpreted this area to have developed in a transtensional regime at ca. 305–295 Ma, where exhumation was driven by the Monte Grighini shear zone (MGSZ). Owing to several similarities between the MGSZ and the transpressive Posada-Asinara shear zone (PASZ) in northern Sardinia and within the framework of the southern European Variscan belt (Matte 2001; Corsini and Rolland 2009; Carosi et al. 2020, 2022; Simonetti 2021 for a review), a re-investigation of the tectonic regime associated with the MGSZ has been performed. Here we present an updated view on the tectono-metamorphic history of the Monte Grighini dome and its non-coaxial deformation, by integrating field observations, meso- and microstructural data, vorticity analysis, *P–T* estimates and in situ U–(Th)–Pb (texturally- and chemically-controlled) geochronology of monazite.

Geological overview of the Variscan belt in Sardinia

Due to the lack of a strong subsequent Alpine age overprint, the segment of the Variscan orogen exposed in Sardinia, Italy, represents a key locality for investigating the southern European Variscan belt (Carosi et al. 2020). Carmignani et al. (1994, 2001, 2015) divided the Variscan basement of Sardinia into three main tectono-metamorphic zones (Fig. 1a). These include: (i) the External Zone or the foreland; (ii) the Axial Zone or the hinterland; and (iii) the Nappe Zone or the hinterland–foreland transition zone.

The Nappe Zone, which comprises most of the metamorphic basement, is subdivided into External and Internal Nappes Zones (Fig. 1a). The boundary between these zones is marked by the Barbagia Thrust, a regional-scale, top-to-the

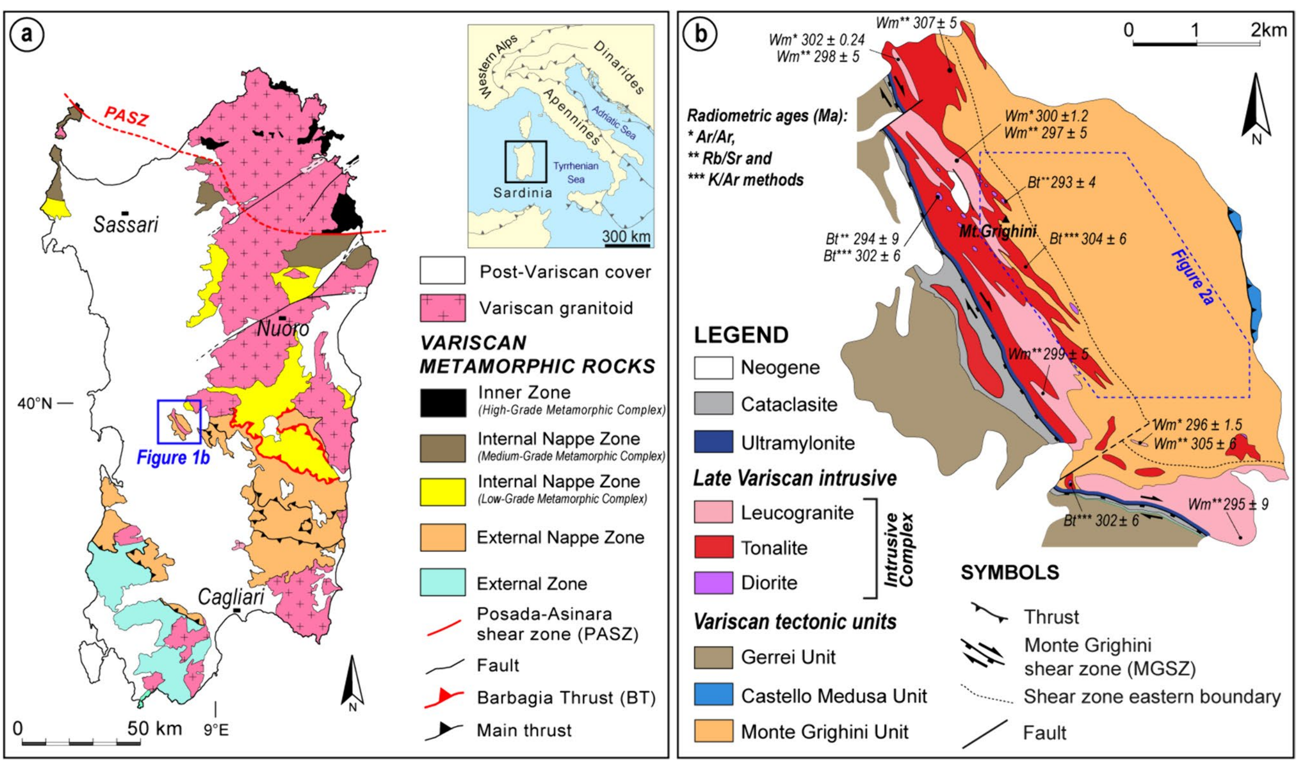

Fig. 1 **a** Tectonic sketch map of Sardinia (modified after Carosi et al. 2020). The blue box marks the location of the investigated area; **b** Simplified geological map of the Monte Grighini dome (modified after Musumeci et al. 2015; Cruciani et al. 2016, 2017). Previous radiometric ages, the method used for dating, and the studied mineralogical phase are shown in the inset (**b**). The dashed blue line indicates the perimeter of the investigated area (Fig. 2a)

S–SW, thrust-sense, ductile to brittle shear zone (Carosi and Malfatti 1995; Conti et al. 1998; Montomoli et al. 2018; Petroccia et al. 2022a, b).

The External Nappe Zone comprises five tectonic units. From the structurally deepest to shallowest, these are: (i) the Monte Grighini Unit, (ii) the Riu Gruppa/Castello Medusa Unit, (iii) the Gerrei Unit, (iv) the Meana Sardo Unit, and (v) the Sarrabus Unit (Carmignani and Pertusati 1977; Carmignani et al. 1982, 1994, 2012; Carosi and Pertusati 1990; Carosi et al. 1991; Loi et al. 1992, 2023; Conti et al. 1999, 2001; Barca et al. 2003; Funedda et al. 2011, 2015; Cocco et al. 2018, 2022). The Gerrei, Meana Sardo, and Sarrabus units underwent regional greenschist-facies metamorphism, as constrained by illite and chlorite crystallinity (Franceschelli et al. 1992; Carosi et al. 2010; Montomoli et al. 2018) and recently confirmed, by Raman spectroscopy on carbonaceous material (RSCM) on samples from the Meana Sardo Unit (Petroccia et al. 2022a,c). The deepest unit of the External Nappe Zone, i.e., the Monte Grighini Unit, reached medium-grade metamorphic conditions (i.e., amphibolite-facies; Musumeci 1992; Carmignani et al. 1994; Cruciani et al. 2016), within the core of the largest tectonic culmination, i.e., the Flumendosa Antiform. In a more external position (i.e., the External Zone or Foreland), Cruciani et al. (2022a, b) interpreted the Mt. Filau orthogneiss to be a similar example of a LP–H*T* metamorphic complex, like the Monte Grighini dome.

Geology of the Monte Grighini dome

The Monte Grighini dome (Musumeci 1992; Musumeci et al. 2015; Fig. 1b) consists of three tectonic units that, structurally from the bottom to the top, are (i) the Monte Grighini Unit (MGU), (ii) the Castello Medusa Unit, and (iii) the Gerrei Unit. The MGU comprises amphibolite-facies felsic metavolcanics (i.e., the Truzzulla Formation), metasediments (i.e., the Toccori Formation), and intrusive granitic rocks (Musumeci et al. 2015). The Truzzulla Formation (Fm.) consists of Upper Ordovician (447 ± 4.3 Ma) metavolcanics, metarkoses, and arkosic metasandstones (Cruciani et al. 2013). The Toccori Formation comprises metapelitic phyllites passing into hornfels adjacent to granitic intrusions (Cruciani et al. 2013, 2017) of the Intrusive Complex (IC; Cruciani et al. 2016). The IC is a NW–SE trending, sub-vertical intrusive body characterized by ages of 303 ± 18 Ma and 305 ± 16 Ma (Rb/Sr isochron) for a two-mica leucogranite and monzogranite, respectively (Carmignani et al. 1987; Fig. 1b). K/Ar, Ar/Ar, and Rb/Sr dating of igneous biotite and muscovite yielded cooling ages ranging between 305 and 295 Ma (Del Moro et al. 1991; Musumeci 1992; Fig. 1b).

The MGU records a polyphase deformation history (Musumeci 1992; Cruciani et al. 2016). The main foliation (S_2) is a NW–SE striking continuous schistosity that dips steeply both to the NE and SW. The S_2 foliation is characterised by syn-metamorphic pervasive ductile shearing (Cruciani et al. 2016). According to Musumeci (1992) and Cruciani et al. (2016), the D_1 and D_2 phases are associated with deformation that occurred during nappe stacking. D_3 folds are represented by large-scale NW–SE trending upright antiforms and synforms, related to the development of a late, regional-scale folding event. The D_3 phase is associated with syn-kinematic blastesis of chlorite, indicating deformation under lower grade metamorphic conditions (Cruciani et al. 2016). The D_4 phase corresponds to a kilometre-wide NW–SE trending dextral transtensional shear zone located in the western sector of the MGU (Musumeci 1992; Columbu et al. 2015; Cruciani et al. 2016, 2017; Musumeci et al. 2015; Fig. 1b). This shear zone, i.e., the MGSZ (Elter et al. 1990; Fig. 1b), is associated with a steeply SW dipping foliation and subhorizontal to gently plunging object and mineral lineations (Musumeci et al. 2015). The MGSZ is marked by syn-kinematic sub-vertical emplacement of the IC, with a dextral sense of movement (Musumeci 1992). Along the westernmost and the south-westernmost sector of the Monte Grighini dome, a NW-trending fault containing cataclastic rocks (Fig. 1b) marks the contact between the MGU and the overlying Gerrei Unit (Musumeci et al. 2015). A thrust contact in the northeastern sector of the Monte Grighini dome (Fig. 1b) marks the boundary between the dome and the Castello Medusa Unit.

Field data and mesoscale observations

In order to describe the structural architecture of the studied area without bias from the previous investigations, the sequence of deformation events and structural elements are numbered relative to the principal event (e.g., S_p, S_{p-1}), where the subscript ‘p’ denotes ‘principal’. Abbreviations are: (S) for foliation surfaces or axial plane foliation; (A) for fold axes; (L) for object stretching lineations; (F) for folds; and (D) for deformation phases. Four ductile deformation phases were observed. Figure 2a and b shows the geological map and the cross-section based on fieldwork performed as part of this study, integrated with the existing cartographic data (Musumeci et al. 2015). Figure 2c displays stereoplots of the main structural elements.

The oldest detectable deformation phase (D_{p-1}) is denoted by a relict foliation (S_{p-1}), observed only in the hinges of D_p folds (Fig. 3a). The D_p tectonic phase is characterised by deformation that is partitioned into low- and high-strain zones. Low-strain zones are domains associated with tight to isoclinal folding (Fig. 3a), where the A_p fold axes are scattered with general W–E to NW–SE plunges (Fig. 2c) and by the occurrence of an anastomosing pattern of deformation

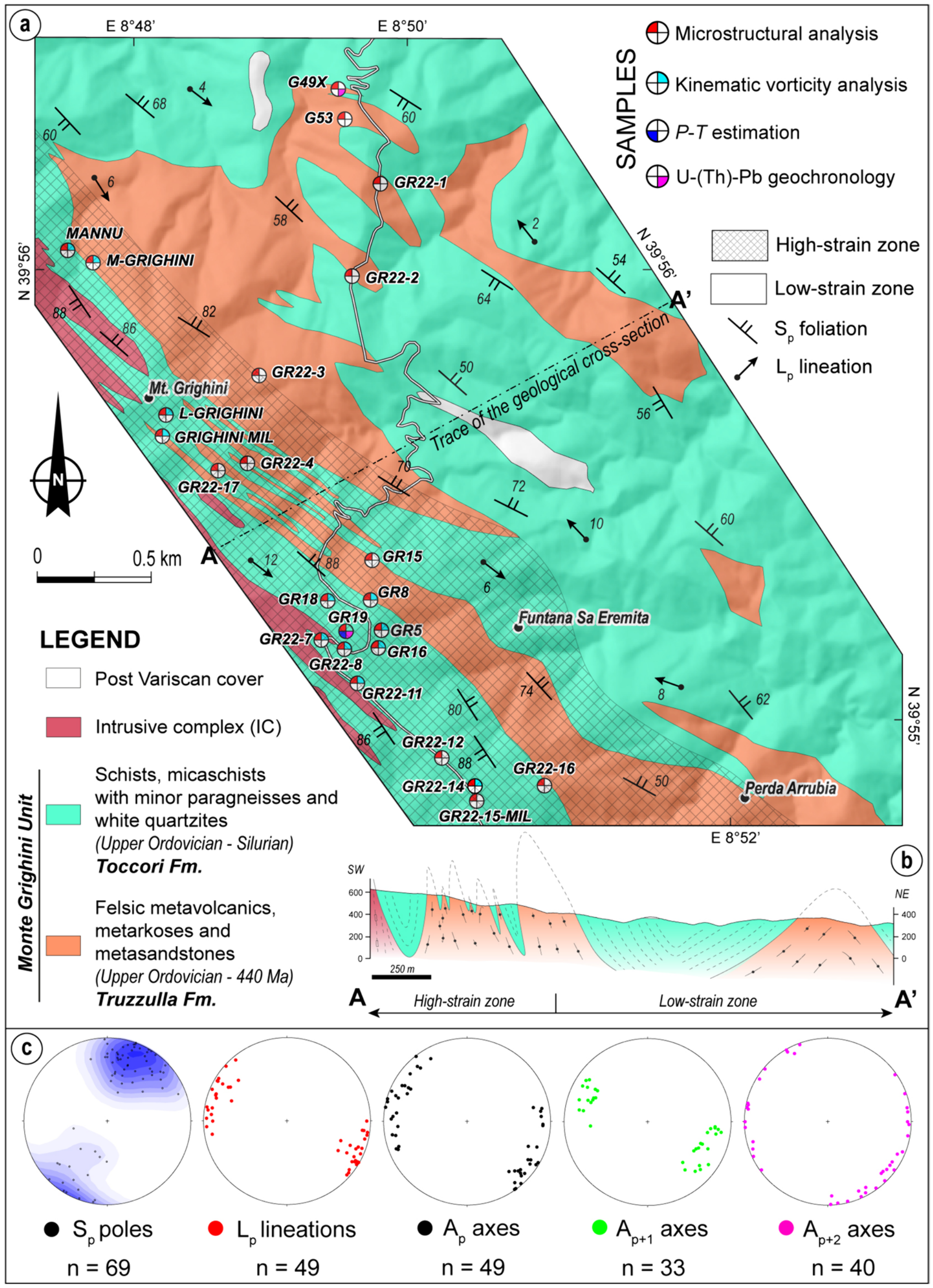

Fig. 2 **a** Simplified geological map of the investigated sector of the dome (modified after Musumeci et al. 2015; see Fig. 1b for its location). See the geological map from Musumeci et al. (2015) for a complete overview of the structural elements of the Monte Grighini dome. Samples selected for study and the corresponding types of analysis are shown; **b** SW–NE oriented geological cross-section; **c** Stereoplots (equal area, lower hemisphere projections) of the main structural elements

with centimetre to metre thick milonitic domains separating unsheared or weakly deformed domains. In contrast, mylonitic high-strain zones are characterized by LS tectonites containing well-developed kinematic indicators, with the occurrence of rootless folds. The F_p folds are associated with an S_p an axial planar foliation, representing the main structural elements in the study area (Fig. 3a). The sub-vertical S_p foliation (Fig. 2c) generally strikes NW–SE and dips moderately to steeply to the N–NE and to S–SW (Fig. 3b). S_p changes from a disjunctive cleavage in the northeastern part of the area, to a continuous mylonitic foliation (Fig. 3c) toward the westernmost sector. Thus, moving toward the MGSZ, the strain increases progressively and is characterised by an increase of the degree of non-coaxial deformation (i.e., the high-strain zone). The L_p object lineation is defined by elongated biotite, sillimanite and muscovite crystals and by millimetre to centimetre-scale quartz rods. L_p generally plunges gently to sub-horizontal (~0°–30°) to the NW and SE (Figs. 2c, 3b). The presence of a sub-vertical or moderate dipping angle S_p foliation, parallel to the mylonitic foliation in the high-strain zone, and F_p fold axes, parallel to the sub-horizontal L_p mineral lineation, is compatible with

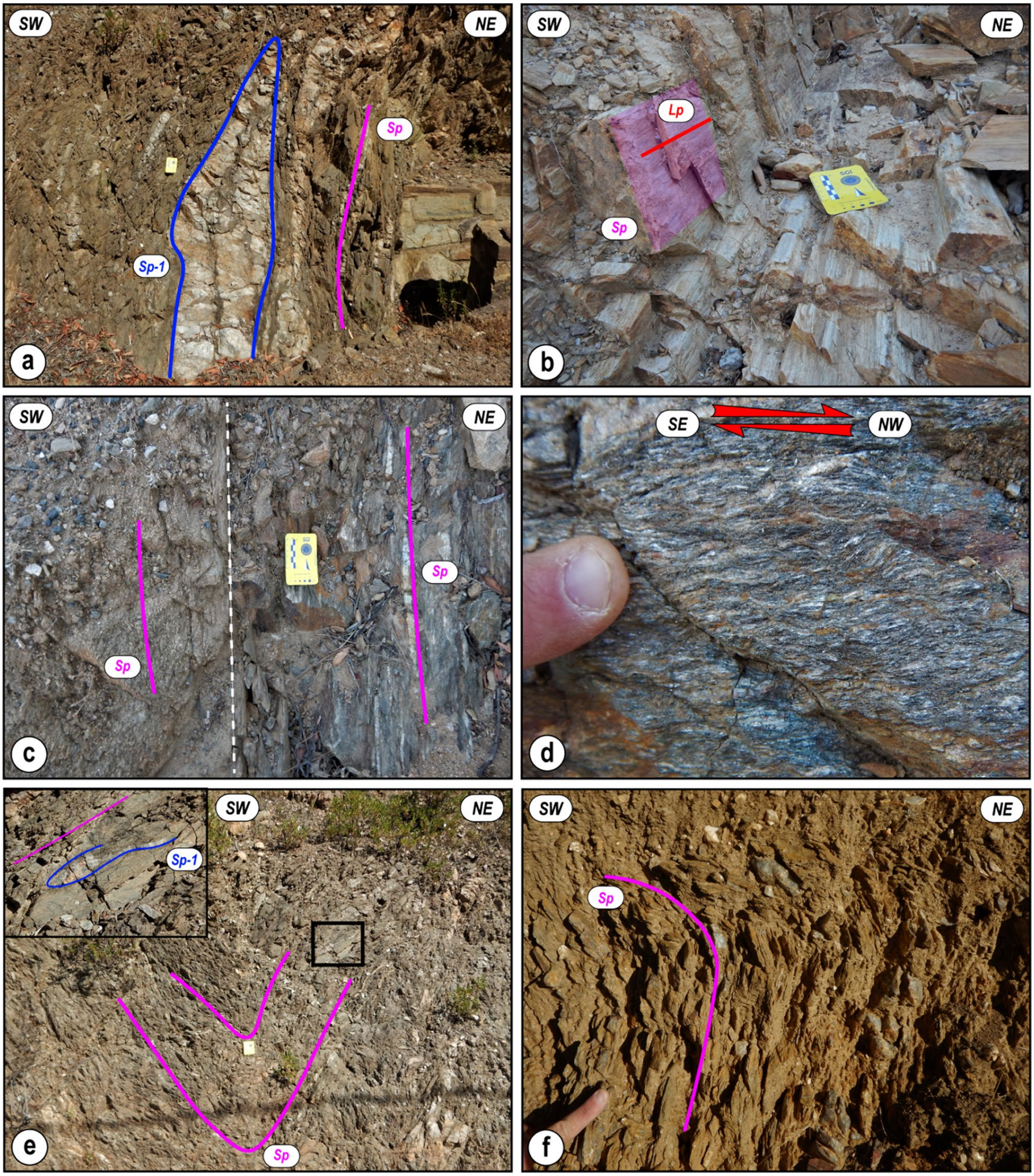

Fig. 3 **a** Outcrop view of F_p folds in the Toccori Formation deforming an older relict foliation (S_{p-1}); **b** L_p sub-horizontal object lineation along the moderately dipping S_p is displayed; **c** Sub-vertical S_p foliation. The contact between the intrusive rock belonging to the IC (on the left) and the Toccori Formation schist (on the right) is parallel to the S_p (the yellow card indicating the scale is 5 cm in length). The white dashed line indicates the boundary between the intrusive rock and the schist; **d** Mylonite from the Toccori Formation at the mesoscale: *C′*–S fabric is indicative of a dextral sense of shear; **e** upright F_{p-1} fold, deforming the S_p attitude (the yellow card indicating the scale is 5 cm in length). The inset shows an enlarged view of the F_p fold and the S_{p-1} foliation located in the NE limb of the F_{p+1} fold is displayed; **f** Outcrop showing late open folds (F_{p+2}) with sub-horizontal axes and axial planes, deforming the S_p foliation

the simultaneous development of D_p high-strain and F_p fold domains linked to the MGSZ activity. Shear sense indicators were observed within the high-strain zones on sections parallel to the XZ plane of the finite strain ellipsoid (the *X* axis is defined by the orientation of L_p) and are coeval with D_p. They are mainly represented by S–*C* and S–*C′* fabrics (Fig. 3d) and rotated porphyroclasts. Kinematic indicators, both at the meso- and microscale, point to a dextral displacement in agreement with the previous interpretations (Elter et al. 1990; Musumeci 1992). F_{p+1} folds affect the S_p foliation and commonly show gentle to slightly asymmetric upright geometry (Fig. 3e), with metre to decametre-scale wavelengths. Locally, kink and/or chevron-type F_{p+1} folds are observed. A_{p+1} fold axes trends are similar to the A_p fold axes and L_p object lineations but their plunges are greater (Fig. 2c). The F_p–F_{p+1} fold interference pattern shows parallel axes and sub-orthogonal axial planes (Fig. 3e). A D_{p+1} crenulation cleavage (S_{p+1}) is locally recognisable. D_{p+2} produced gentle to open F_{p+2} folds with sub-horizontal axes and axial planes (Fig. 3f). The trend of shallowly plunging A_{p+2} axes varies from E–W to NW–SE with a very high degree of dispersion (Fig. 2c). The D_{p+2} deformation phase is not associated with the development of foliations and lineations.

The late Fp + 2 gentle folds modified the steeply dipping attitude of the main Sp causing a different dip that alternate between the SW and NE. Kinematic indicators, on the different dipping limbs of the Fp + 2 folds, indicate top-to-the-NW or to-the-SE sense of shear respectively (see Supplementary Material S6).

Microstructures

We performed microstructural investigations on 24 samples (see Fig. 2a for sample locations). Foliations have been classified according to Passchier and Trouw (2005). Quartz dynamic recrystallisation microstructures are defined according to Stipp et al. (2002a, b) and Law (2014). Mineral abbreviations are after Warr (2021).

Porphyroids (metamorphosed volcanic felsic rocks or tuffs) and metavolcanic rocks of the Truzulla Formation are deformed and characterised by a porphyroclastic microstructure (Fig. 4a) with millimetre-sized K-feldspar (Fig. 4b) and subordinate plagioclase porphyroclasts. The S_p cleavage is marked by white mica, biotite, and rare chlorite. Quartz and phyllosilicate grains are oriented parallel to the main schistosity (S_p) wrapping around feldspar porphyroclasts (Fig. 4b). Sigma- and delta-type asymmetric K-feldspar porphyroclasts (Fig. 4b) and asymmetric strain shadows around clasts, indicate a dextral sense of shear. Quartz shows lobate grain boundaries suggesting dynamic recrystallisation by grain boundary migration (GBM), indicative of temperatures > 500 °C (Law 2014). In some samples, overprinting by subgrain rotation (SGR) recrystallisation indicates lower temperatures.

Metasediments belonging to the Truzulla Formation are characterised by a disjunctive foliation (S_p; Fig. 4c), sub-parallel cleavage domains, and a continuous schistosity mainly defined by biotite, white mica, and quartz. The S_p foliation wraps around garnet and staurolite (Fig. 4c). A sporadic internal foliation (S_{p-1}), consisting of oriented quartz, white mica, ilmenite, and graphite, varies from discordant to concordant with the external foliation (Fig. 4b). This suggests that garnet and staurolite may be inter- to early syn-tectonic (syn-S_p) with respect to S_p (i.e., their growth either occurred between $D_{p\text{-}1}$ and D_p or during the early stage of D_p). Quartz has irregular, lobate, and ameboid grain boundaries compatible with GBM recrystallisation. Samples collected within the high-strain zone display a dextral sense of shear, marked by mica-fish (Fig. 4d), S–*C* and S–*C′* fabrics, and asymmetric strain shadows around porphyroclasts.

Schists and paragneisses from the Toccori Formation are characterised by a continuous foliation defined by the alternating quartzo-feldspathic and muscovite–biotite–sillimanite-rich layers (Fig. 4e). Prismatic sillimanite, biotite, and white mica define the S_p schistosity (Fig. 4e). Fine-grained fibrolite (Fig. 4e), kinematic indicators, such as S–*C* and S–*C′* fabrics (Fig. 4e) and mica-fish, are also present. Quartz shows evidence of GBM and, more rarely, chessboard extinction (Fig. 4f).

Methods

Kinematic vorticity analysis

The non-coaxiality of flow in shear zones is commonly expressed by the kinematic vorticity number, W_k (Xypolias 2010), which can be estimated using several kinematic vorticity analysis techniques. W_k describes instantaneous deformation and is the ratio between the magnitude of the vorticity vector and the difference between the intermediate and minimum principal stretching rates, whereas the mean kinematic vorticity number W_m is used when referring to finite deformation (Xypolias 2010). Vorticity analysis is based on information about progressive deformation or flow parameters, such as the incremental strain, instantaneous stretching axes (ISA), and flow apophysis, and the relative rotation of line and plane structures during deformation. In any type of two-dimensional flow, it is possible to recognize two lines, defined as the flow apophyses (*A*1 and *A*2), that do not undergo rotation. The component of simple shear decreases as the angle between *A*1 and *A*2 increases, such that: the flow apophyses are orthogonal in pure shear flow and coincide with each other in simple

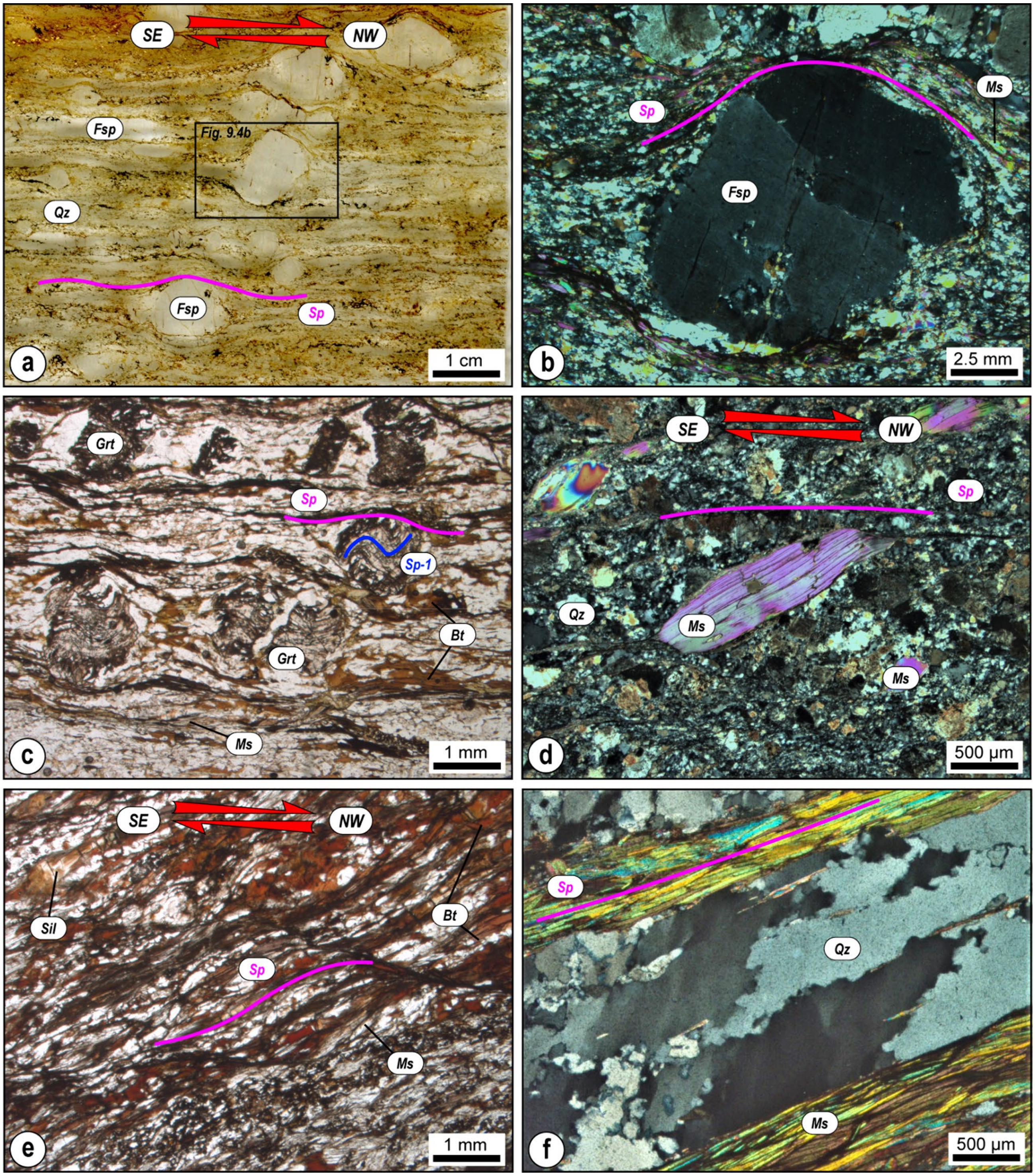

Fig. 4 **a**, **b** Sheared metavolcanic rock belonging to the Truzulla Formation showing a dextral sense of shear. σ-type porphyroclast shows a dextral sense of shear; **c** garnet porphyroclast showing an internal foliation S_{p-1} (blue line) both discordant and locally concordant with the S_p foliation. Garnet is wrapped by the main foliation S_p (violet line) defined by white mica + biotite; **d** mica-fish in Truzulla Formation rock showing a dextral movement; **e** *C′*–S fabric in sillimanite-bearing schist, indicating a dextral sense of shear; **f** dynamically recrystallised quartz showing lobate and irregular grain boundaries indicative of GBM recrystallization

shear flow. For general shear flow, $A1$ and $A2$ define an acute angle in the direction of the flow.

One of the most common assumptions when carrying out kinematic vorticity analysis is that of simple shear, i.e. plane strain and the deformation is monoclinic (Passchier 1998). The other important assumption is of steady-state deformation, or that the estimated W_k value represents an average W_k over the deformation interval during which the applied structure or fabric formed. In addition, constant volume is commonly assumed, which will, for simplicity, also be assumed here. The nominal error for kinematic vorticity analysis is ± 0.1 (Tikoff and Fossen 1995). A comparison of different possible systematic error sources indicates that for medium to low mean kinematic vorticity numbers ($W_m < 0.8$), the vorticity data minimum systematic error is ± 0.2 (Iacopini et al. 2011).

Progressive pure and simple shear are described by $W_k = 0$ and $W_k = 1$, respectively. The progressive simple and pure shear components contribute equally to the deformation when $W_k = 0.71$ (Law et al. 2004; Passchier and Trouw 2005; Xypolias 2010). The consequence of having a pure shear component within a shear zone is that the shear zone material is extruded in the X direction parallel to the measured object lineation. The kinematics of flow, namely, the components of pure and simple shear acting simultaneously during deformation (see Fossen and Cavalcante 2017; Xypolias 2010, for reviews) expressed by the kinematic vorticity number W_m, were estimated using two independent kinematic vorticity gauges: the C' shear band method (Kurz and Northrup 2008; Gillam et al. 2013) and two different porphyroclast-based methods: (a) the porphyroclast aspect ratio method (PAR; Passchier 1987; Wallis et al. 1993) and (b) the rigid grain net method (RGN; Jessup et al. 2007).

The C' shear band method is based on measurements of the orientation of C' planes with respect to the boundaries of the MGSZ (ν angle). Theoretically, C' planes nucleate as the bisector of the angle between the two flow apophyses (Platt and Vissers 1980; Kurz and Northrup 2008; Xypolias 2010). Based on this assumption, the kinematic vorticity number is given by $W_m = \cos 2\nu$ (Kurz and Northrup 2008). As each element in a flow tends to rotate, including C' planes, it is necessary to consider the spread of ν value measurements to estimate the initial amplitude of the angle during the formation of the C' planes. Gillam et al. (2013) proposed to use an average ν value for low-strain rocks or in cases where C' planes developed at a late stage of the deformation history and nucleated in a stable orientation; in such cases, C' planes undergo little or no rotation after inception. For highly strained rocks, deformed in long-lasting shear zones, as in the present study case, the maximum value of ν is preferable since it better approximates the nucleation angle of C' planes (see Kurz and Northrup 2008).

Porphyroclast-based methods have proved to be extremely useful for quantifying vorticity in ductile shear zones, but their accuracy is affected by several factors (see Xypolias 2010 for a review): (i) rigid clasts should be embedded in a homogeneously deforming matrix; (ii) the shape of clasts should not change during deformation due to recrystallisation or fracturing; (iii) the sample should consist of a population of clasts with a range of aspect ratios (Law et al. 2004); (iv) the strain must be sufficient to allow clasts to reach a stable sink position. If these conditions are not met, porphyroclast-based methods tend to overestimate W_m values (e.g. Bailey et al. 2004). For both porphyroclasts-based methods, measurements were conducted using the Ellipse-Fit 3.8.0 software (Vollmer 2015). The results were plotted on both PAR (Passchier 1987; Wallis et al. 1993) and RGN (Jessup et al. 2007) graphs. In detail, both the PAR and RGN methods require measurement of the axial ratio of porphyroclasts (R) and the angle (ϕ) between the long axis of the rigid grain and the mylonitic foliation (Passchier 1987; Wallis et al. 1993). For simple shear, particles will rotate permanently for all realistic porphyroclast shapes, but for subsimple shear, particles with an aspect ratio above a critical aspect value (R_c) will rotate into a stable position and then stay fixed (Jeffery 1922). To find Rc we plot the porphyroclast aspect ratio against the angle between the clast's long axis and the foliation as observed in the XZ plane. This method is commonly referred to as the PAR method (Passchier 1987). For high-strain rocks, the flow plane is considered to be parallel to the straight tails of porphyroclasts; although most published studies take the trace of macroscopic mylonitic foliation as the reference frame (Xypolias 2010). Theoretically, on such graphs, two fields of behaviour for rotated clasts can be distinguished: (a) a field where the clasts with low shape factor rotate infinitely and hence display a wide range in their long axis orientations; and (b) a field where the clasts rotate slowly (forward or backward). To minimise the uncertainties, two Rc values have been chosen (R_c min and R_c max) and an average vorticity has been calculated using the relation $W_m = (R_c^2 - 1)/(R_c^2 + 1)$. Graphs for natural porphyroclast systems, however, often exhibit a gradual transition rather than an abrupt change between these two fields (e.g. Jessup et al. 2007). The Rigid Grain Net (RGN) is an alternative graphical method for estimating mean kinematic vorticity number (W_m) from the shape and orientation of porphyroclasts that are inferred to represent variably rotating rigid objects in a flowing matrix (Jeffery 1922). proposed by Jessup et al. (2007). The RGN method uses a modification of the original plot proposed by Passchier (1987) for PAR analysis and includes a set of semi-hyperbolas plotted in both positive and negative space at 0.025 intervals of Wm that are mathematically equivalent to a hyperbolic net (Xypolias 2010). Each clast is plotted on the rigid grain net according to its shape factor (B^*) and the angle made between its long axis and foliation (θ). These semi-hyperbolas transition into vertical lines to define the maximum B^* as the critical threshold (R_c) between grains that rotate infinitely and those that reach a stable-sink position. In other words, grains with B^* values below R_c rotate freely (i.e., they define a vertical boundary outside of the semi-hyperbola) and do not develop a preferred orientation, while grains with B^* values above R_c have limited rotation (i.e., they lie within the semi-hyperbola). W_m is estimated directly from the RGN based on where the critical shape factor (B^*) equals the aspect ratio of the porphyroclast at the critical threshold (R_c). Therefore, each sample's estimated Rc is equal to its estimated W_m. The validity of RGN analysis relies on two assumptions (e.g. Xypolias 2010): (i) the plane of reference for measurement is parallel to lineation and the pole to foliation; and (ii) the plane of reference for measurement is normal to the vorticity vector. These assumptions define a monoclinic shear zone and, therefore, require that the shear zone to which the methods are applied have a history dominated by monoclinic deformation. It is important to note that we assume that $W_k = W_n = W_m$ for samples dominated by monoclinic deformation.

About the fifteen analysed samples (see Fig. 2a for sample location), twelve have been investigated by the C' shear band method, due to the presence of C' planes, whereas only 3 samples have been analysed using porphyroclast-based methods. Only samples with a considerable number of freely rotating clasts (> 50), lacking internal deformation, were chosen.

Phase equilibrium modelling

Pressure–temperature (P–T) conditions were estimated using phase equilibrium modelling. The investigated sample (GR19) was selected because it shows a well-developed equilibrium mineral assemblage, fundamental for constraining P–T conditions, and also contains both white mica and biotite. The construction of equilibrium phase diagrams depends on the choice of a bulk composition representative of the sample or a specific stage in its metamorphic history (reactive bulk composition), the use of an appropriate chemical system, and the selected thermodynamic dataset and solution models.

The bulk composition used for modelling can influence the topology and phase proportions predicted in a P–T phase diagram (e.g., Stüwe and Powell 1995; Palin et al. 2016). In this study, a local bulk composition was determined using an X-ray map of a representative area of the thin section (~ 45 × 30 mm), chosen based on the size of the smallest grains. X-ray compositional maps and quantitative chemical analyses were performed using the electron probe microanalyser (EPMA) JEOL JXA-8200 superprobe at the Institute of Geological Sciences (University of Bern). X-ray maps of Al, Fe, K, Mg, and Na were acquired in a single scan by wavelength-dispersive spectrometry (WDS), whereas Ca, P, Si, and Ti were measured simultaneously by energy-dispersive spectroscopy (EDS). The program XMapTools v4 (Lanari et al. 2014) was used to process compositional maps, including (i) classification, (ii) analytical standardisation, (iii) structural formulae calculation and (iv) distinction of compositional groups. Mineral structural formulae have been calculated based on 11 oxygens for white mica and biotite and 8 oxygens for plagioclase. Local bulk compositions were generated from the oxide weight-percentage maps by averaging pixels with a density correction (Lanari and Engi 2017).

Pseudosection (or forward) modelling was conducted in the 10-component NCKFMASHTO (Na_2O–CaO–K_2O–FeO–MgO–Al_2O_3–SiO_2–H_2O–TiO_2–Fe_2O_3) system. MnO was not considered because all phases contained negligible manganese concentrations. Only total Fe is determined by EPMA, while Fe oxidation states (Fe^{2+} and Fe^{3+}) are not measured. XMapTools considers all Fe in muscovite and biotite to be Fe^{2+} and thus the bulk composition calculated for sample GR19 assumed total Fe as Fe^{2+}. However, biotite and muscovite in pelitic rocks contain appreciable amounts of Fe^{3+} (Forshaw and Pattison 2021 and references therein). To account for this and to model in the NCKFMASHTO system, a bulk XFe^{3+} (= $Fe^{3+}/(Fe^{3+} + Fe^{2+})$ in moles) for sample GR19 was determined by combining estimates of XFe^{3+} in minerals with modal abundances (e.g., Forshaw et al. 2019). Modal abundances of biotite and muscovite were extracted from XMapTools. Ilmenite is the main Fe-oxide in sample GR19, therefore XFe^{3+} was estimated to be 0.11 in biotite and 0.49 in muscovite (Forshaw and Pattison 2021). Bulk XFe^{3+} was calculated to be 0.10, which is lower than the whole-rock $XFe^{3+} = 0.23$ of the worldwide median pelite (Forshaw and Pattison 2023). However, the latter is based on XFe^{3+} measurements from titration which should be considered a maximum due to pre-analysis oxidation during grinding (Fitton and Gill 1970). An $XFe^{3+} = 0.10$ is consistent with the chosen thermodynamic dataset and solution models that give a Fe-oxide assemblage (ilmenite) that is matched by the phase diagrams (see results below and discussion in Forshaw and Pattison 2021).

Phase diagrams were computed using Theriak–Domino (De Capitani and Brown 1987; De Capitani and Petrakakis 2010), the internally consistent dataset of Holland and Powell (2011; update ds62; February 2012), and associated solution models of White et al. (2014), except for the plagioclase model where the model of Holland et al. (2021) was used. The thermodynamic dataset and solution models were chosen because the solution models incorporate enough Fe^{3+} end members to simulate Fe^{3+}-bearing phase equilibria (Forshaw and Pattison 2021).

The results of phase equilibrium modelling were compared with those of the conventional Ti-in-Bt geothermometer (Henry et al. 2005). The calibration of Henry et al. (2005) is applicable in peraluminous rocks containing graphite and a Ti reservoir, such as rutile or ilmenite, at low-to-medium pressures (P = 0.4–0.6 GPa) and a T range of 480–800 °C. This geothermometer has an estimated precision of ± 24 °C.

In situ monazite U–(Th)–Pb geochronology

In situ U–(Th)–Pb dating of monazite, integrated with its chemical and microstructural characterisation, was used to constrain the timing of metamorphism (see Kohn et al. 2017 for a detailed review of this technique). Using a scanning electron microscope at the University of Turin (Italy), we investigated the locations of grains, their internal features (e.g., inclusions), and their textural position. Each monazite crystal was then analysed using the JEOL 8200 Super Probe electron microprobe hosted at the Department of Earth Sciences "A. Desio" of the University of Milan (Italy) to elucidate their chemical composition and test for the presence of compositional zoning. This step was necessary in order to correctly interpret monazite grains and their relative ages. Isotopic monazite dating was conducted in situ, on 30 µm-thick thin sections, using Laser Ablation Inductively Coupled Plasma-Mass Spectrometry (LA-ICP-MS) at the Università degli Studi di Perugia (Italy). This facility consisted of a Teledyne/Photon Machine G2 LA device equipped with a HelEx2 two-volumes cell and coupled with a Thermo-Fisher Scientific quadrupole-based iCAP-Q ICP-MS. Monazite crystals were analysed using a circular laser beam of 8–10 µm diameter, a frequency of 10 Hz and a laser fluence on the sample surface of ~ 3.5 J/cm^2. Oxides were checked on the NIST SRM 612 standard by monitoring and maintaining the ThO/Th ratio below 0.005. The Delaware standard (424.9 ± 0.8 Ma; Aleinikoff et al. 2006) was used as a calibrator (Supplementary Information S1). The Moacir (or Moacyr, 507.7 ± 1.3 Ma ($^{207}Pb/^{235}U$) and 513.6 ± 1.2 Ma ($^{206}Pb/^{238}U$); Gonçalves et al. 2016) and Manangotry (555 ± 2 Ma, Horstwood et al. 2003; 537 ± 14 Ma, Montel et al. 2018) monazite standards were used as quality controls. Data reduction was performed in Iolite4 (Paton et al. 2011) utilising the VizualAge_UcomPbine data reduction scheme (Chew et al. 2014). All subsequent data processing and plotting was done using the software ISOPLOT (Ludwig 2003).

Results

Kinematics of ductile flow

The results of the kinematic vorticity analysis are reported in Table 1. Twelve samples (see Fig. 2a for sample location) analysed with the C' shear band method gave kinematic vorticity numbers (W_m) ranging from 0.41 to 0.50, with a mean of 0.46. Vorticity analysis using the porphyroclasts-based methods on three samples (GR22-5, L-GRIGHINI

Table 1 Results of kinematic vorticity investigations: number of data (N), angle between C' planes and the shear zone boundary (ν), W_m value (W_m), mean value of W_m in a range (W_m) and the average of its range (W_m mid); minimum critical axial ratio (R_c min), maximum critical axial ratio (R_c max), minimum value of W_m (W_m min), maximum value of W_m (W_m max), mean value of W_m (W_m mid)

Kinematic vorticity analysis											
Sample name	C' shear bands method			Rigid grain net method (RGN)			Porphyroclasts aspect ratio method (PAR)				W_m mid
	N	ν angle (°)	W_m	N	W_m	W_m mid	R_c min	R_c max	W_m min	W_m max	
GR22-5	–	–	–	68	0.39–0.44	0.42	1.48	1.70	0.37	0.49	0.43
GR22-7	23	32	0.44	–	–	–	–	–	–	–	–
GR22-8	10	31	0.47	–	–	–	–	–	–	–	–
GR22-11	15	30	0.50	–	–	–	–	–	–	–	–
GR22-14	27	30	0.50	–	–	–	–	–	–	–	–
L-GRIGHINI	–	–	–	64	0.43–0.47	0.45	1.63	1.81	0.45	0.53	0.49
M-GRIGHINI	–	–	–	60	0.37–0.45	0.41	1.52	1.72	0.4	0.49	0.45
GR5	20	32	0.44	–	–	–	–	–	–	–	–
GR8	22	33	0.41	–	–	–	–	–	–	–	–
GR9	10	32	0.44	–	–	–	–	–	–	–	–
GR16	11	30	0.50	–	–	–	–	–	–	–	–
GR18	6	33	0.41	–	–	–	–	–	–	–	–
GR19	19	31	0.47	–	–	–	–	–	–	–	–
GRIGHINI MIL	14	30	0.50	–	–	–	–	–	–	–	–
MANNU	16	31	0.47	–	–	–	–	–	–	–	–

and M-GRIGHINI) gave W_m values between 0.37–0.47 and 0.37–0.53 for RGN and PAR, respectively. The datasets collected by the two porphyroclast-based methods are comparable with results using the *C′* shear bands approach. Taking into account all results obtained by different methods, the W_m values range between 0.3 and 7–0.53 (Fig. 5).

Although we used different methods, the resulting kinematic vorticity number values are relatively homogeneous and do not show a significant variation with the degree of strain. The obtained kinematic vorticity number values indicate that the MGSZ experienced general shear (Forte and Bailey 2007) during deformation, which involved 77–64% pure shear and 23–36% simple shear components (Fig. 5). Green bar represents the range of W_m values obtained in this study for the MGSZ.

Mineral composition

Sample GR19 is a sillimanite-bearing mylonitic schist (Fig. 6a) from the Toccori Formation (see Fig. 2a for the sample location) showing syn-kinematic growth of micas and sillimanite. GR19 contains (Fig. 6b; area% = vol%, estimated from XMapTools): quartz (36%), white mica (26%), biotite (22%), sillimanite (14%), with plagioclase and ilmenite as the main accessory minerals (2% in total). Selected mineral compositions for biotite and white mica in sample GR19, derived both from the XMapTools and WDS spot analysis, are reported in Table 2. Representative analyses of plagioclase are provided in Supplementary Material S2.

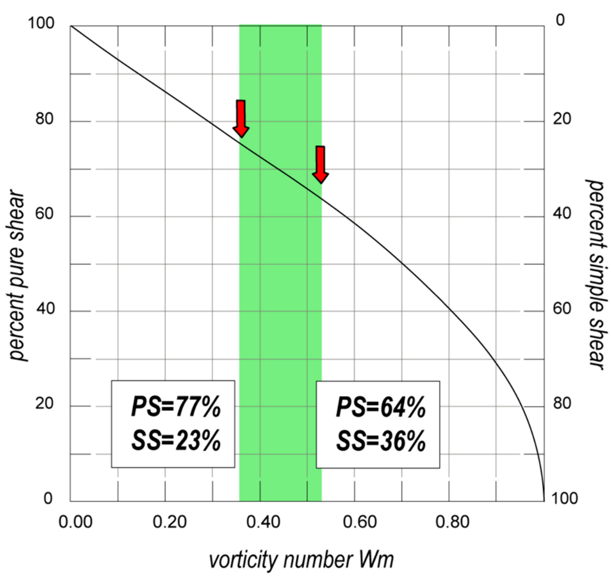

Fig. 5 Relationship between kinematic vorticity number W_m and the percentage of pure shear (PS) and simple shear (SS) (modified after Law et al. 2004)

White mica is a muscovite with minor pyrophyllite content. It is homogeneous in composition, with mean Si contents of 3.04 ± 0.03 a.p.f.u. and *X*Mg (= Mg/(Mg + Fe^{tot})) of 0.42 ± 0.04. Whilst two generations of biotite can be distinguished using microstructural criteria (Fig. 6a), these different generations are compositionally similar. Using the Rieder et al. (1999) classification, biotite is classified mainly as biotite with high Al, plotting on the siderophyllite-eastonite solid solution vector with intermediate *X*Mg. Biotite parallel to the S_p shows *X*Mg of 0.39 ± 0.01, whereas the post-kinematic (i.e., post-Dp) biotite displays *X*Mg of 0.35 ± 0.02. The Ti a.p.f.u. in biotite does not change with its structural position and has a mean value of 0.14 ± 0.03. Plagioclase is albitic in composition (*X*An = 0.04–0.07).

P–T constraints

Figure 6c and d shows the *P–T* equilibrium phase diagram for sample GR19, calculated for 0.1–1.0 GPa and 500–700 °C. The sillimanite-in curve is located in the pressure range of ~ 0.3–0.7 GPa and between ~ 560–700 °C. Rutile is stable above the upper sillimanite-in line, while ilmenite is predicted in the sillimanite stability field. The observed mineral assemblage (labelled as Pl–Ms–Bt–Ilm–Sil; Fig. 6c) is represented by a field restricted by a *P–T* range of 0.3–0.7 GPa and 560–670 °C, delimited by the disappearance of staurolite, the stability boundary of sillimanite, and by the melt-in reaction (Fig. 6c). Predicted compositional isopleths for syn-Sp biotite (*X*Mg = 0.39–0.40) and white mica (Si = 3.03–3.05 a.p.f.u.; *X*Mg = 0.41–0.43) occur within the observed mineral assemblage stability field. The *P–T* condition has been inferred with compositional isopleths thermobarometry.

Similar temperature results (*T* = 625 ± 25 °C) have been obtained using Ti-in-Bt conventional geothermometry (Henry et al. 2005), consistent with the phase diagram results (Fig. 6d).

Monazite textural position and chemistry

Two samples, inside and outside MGSZ (GR19 and G49X, respectively; see Fig. 2a for the sample position), were chosen for in situ geochronology of monazite. Cruciani et al. (2016) have previously investigated the *P–T* conditions of sample G49X. A total of seven monazite grains, two for sample GR19 and five for sample G49X were analysed. Selected analyses of monazite and the spot analysis position are available in Supplementary Material S3 and Fig. 7, respectively.

Monazites from sample G49X are between ~ 40 and ~ 120 µm in length. We analysed three monazites from the quartz, biotite, and white mica-dominated foliation and two monazites (Mnz 6a and Mnz 7b) that occur

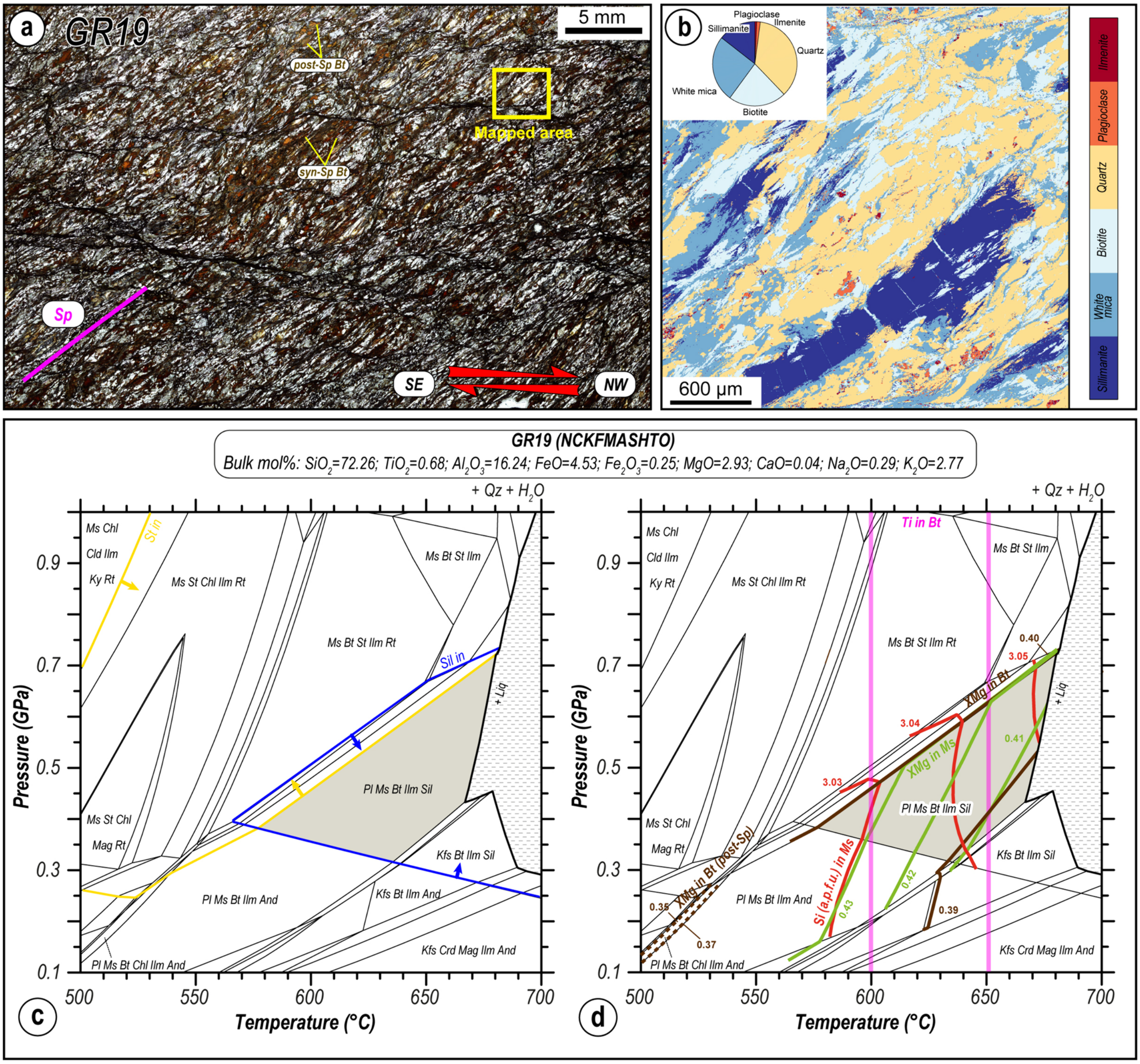

Fig. 6 **a** Thin section scan of sample GR19. The area mapped using EPMA is indicated in yellow; **b** Processed X-ray map of sample GR19 showing the distribution of different minerals. The inset pie-chart depicts the volume % for each phase; **c/d** *P–T* equilibrium phase diagrams for the high-temperature mylonitic sample GR19. The inferred equilibrium assemblage is highlighted in grey; **c** Yellow and blue lines mark the staurolite-out and sillimanite-in reactions, respectively; **d** The intersection of compositional isopleths of biotite and white mica. The temperature obtained from the conventional Ti-in-Bt thermometer is shown by isotemperate purple lines

as inclusions within garnet. The monazites from GR19 are between ~20 and ~60 µm in length. Most of the monazites in this mylonite are very small and difficult to analyse. The crystals located along the Sp foliation are generally within biotite- or sillimanite-rich domains. One monazite (Mnz 11) has an inclusion of sillimanite (Fig. 7). This crystal is particularly interesting because the sillimanite grew during the high-strain shearing event. Backscattered electron (BSE) images show clear zoning in most grains with domains of different grey tones (Fig. 7). X-ray compositional maps reveal that such zoning is controlled by the different distributions of *X*(HREE + Y) and *X*(LREE) + Th (Fig. 7). *X*(HREE + Y) is defined as (HREE + Y)/REE, whereas *X*(LREE) is LREE/REE. The Electron microprobe analysis revealed two chemical domains (I and II), based on Y, Th, and REE content. In sample G49X, Domain I (Fig. 8a, b) is characterised by cores with medium-Y content ranging from 0.022 to 0.035 (a.p.f.u.), low-Th values from 0.01 to 0.026 (a.p.f.u), and *X*(HREE + Y) low amounts varying from 0.044 to 0.067. Domain II (Fig. 8a, b) is characterized by

Table 2 Mean XMapTools map analyses and representative WDS spot analyses for white mica and biotite. Position denotes the representative micro-structural domain from which analyses were taken. Structural formulae were calculated for biotite and white mica based on 11 oxygens per formula unit

Mineral:	Biotite						White Mica		
Position:	Sp			Sp			Sp		
wt%	No. of pixels = 65	No. of pixels = 100	WDS spot analysis	No. of pixels = 88	No. of pixels = 91	WDS spot analysis	No. of pixels = 112	No. of pixels = 225	WDS spot analysis
SiO_2	35.14	34.69	35.05	34.69	34.86	34.51	45.31	44.77	45.14
TiO_2	2.65	2.37	2.50	2.79	2.73	2.88	0.60	0.56	0.71
Al_2O_3	20.02	20.12	19.21	19.36	19.49	19.23	36.19	35.61	36.20
FeO	19.08	19.96	20.50	21.31	21.20	21.56	1.08	1.04	1.10
MgO	6.97	7.37	7.70	6.70	6.67	6.40	0.45	0.44	0.43
CaO	0.06	0.06	0.04	0.05	0.05	0.06	0.05	0.05	0.00
Na_2O	0.13	0.13	0.10	0.13	0.14	0.12	0.83	0.85	0.85
K_2O	9.25	9.41	9.51	9.30	9.32	9.40	9.97	9.80	10.00
Total	93.30	94.11	94.61	94.33	94.46	94.16	94.48	93.12	94.43
Cations									
Si	2.70	2.68	2.70	2.69	2.70	2.69	3.03	3.04	3.04
Ti	0.16	0.14	0.14	0.16	0.15	0.16	0.03	0.03	0.04
AlVI	0.52	0.50	0.45	0.46	0.48	0.46	1.91	1.89	1.91
AlIV	1.32	1.32	1.30	1.31	1.30	1.31	0.96	0.96	0.96
Fetot	1.06	1.13	1.15	1.17	1.17	1.18	0.07	0.06	0.06
Mg	1.01	1.02	1.06	0.98	0.97	0.96	0.05	0.05	0.04
Ca	0.01	–	–	–	–	0.01	–	–	–
Na	0.02	0.02	0.01	0.02	0.02	0.02	0.11	0.11	0.11
K	0.93	0.93	0.94	0.92	0.92	0.94	0.85	0.85	0.85
Sum	7.73	7.74	7.75	7.71	7.71	7.73	7.01	6.99	7.01
*X*Mg	0.39	0.40	0.40	0.36	0.36	0.35	0.42	0.42	0.41

medium–high Y rims/grains, $0.028 < Y < 0.057$ (a.p.f.u.), low-medium Th values from 0.05 to 0.055 (a.p.f.u) and $0.071 < X(\mathrm{HREE} + \mathrm{Y}) < 0.094$. The monazites enclosed in garnet crystals follow the same zoning pattern of many matrix crystals and are chemically similar, in which the cores show medium/low-Y and X(HREE + Y), and the rims are enriched in these same elements. In sample GR19, Domain I (Fig. 8a, b), as documented by X-ray maps (Fig. 7), occurs only in Mnz 11, where a medium-Y ($Y = 0.033$) and low-medium-Th ($Th = 0.013$) core is recognisable. Medium- to high-Y values ($0.042 < Y < 0.061$ a.p.f.u.), medium-Th values from 0.018 to 0.041 (a.p.f.u) and X(HREE + Y) between $0.069 < X(\mathrm{HREE} + \mathrm{Y}) < 0.095$ are well preserved and represent the main features of Domain II (Fig. 8a, b). This domain has been observed both as a continuous rim around cores or as a homogeneous medium–high-Y content grain. The sillimanite inclusion is inside the Y-rich rim correlated with Domain II.

In summary, based on the previously described textural and chemical arguments, monazite, in both samples, shows two main growth domains/generations: (i) Domain I, representing the core of the grains both in garnet and along the mylonitic foliation, with low-medium-Y contents; and (ii) Domain II, forming continuous to rarely discontinuous high X(HREE + Y) rims or homogeneous grains, mainly occurring in the matrix. Considering the resolution of the applied method, we did not detect any significant differences between the monazite chemistry and obtained ages.

In situ U–(Th)–Pb geochronology and ages

The measured isotopic data are reported in Supplementary Material S4 (see Fig. 7 for the laser spot analysis position). A total of seven monazite grains covering the whole textural–chemical variability were selected for in situ dating, and analyses were collected from a total of 13 spots (10 for sample G49X and 3 for sample GR19). Results are plotted on a $^{206}Pb/^{238}U$ versus $^{207}Pb/^{235}U$ concordia diagram (Fig. 8c, d). The concordia calculation gives ages of 321 ± 3.3 and 311 ± 7.3 Ma for G49X and GR19, respectively (Fig. 8c, d). The monazite grain within a sillimanite inclusion (Sample GR19 in Mnz 11) produced similar ages of 315–310 Ma.

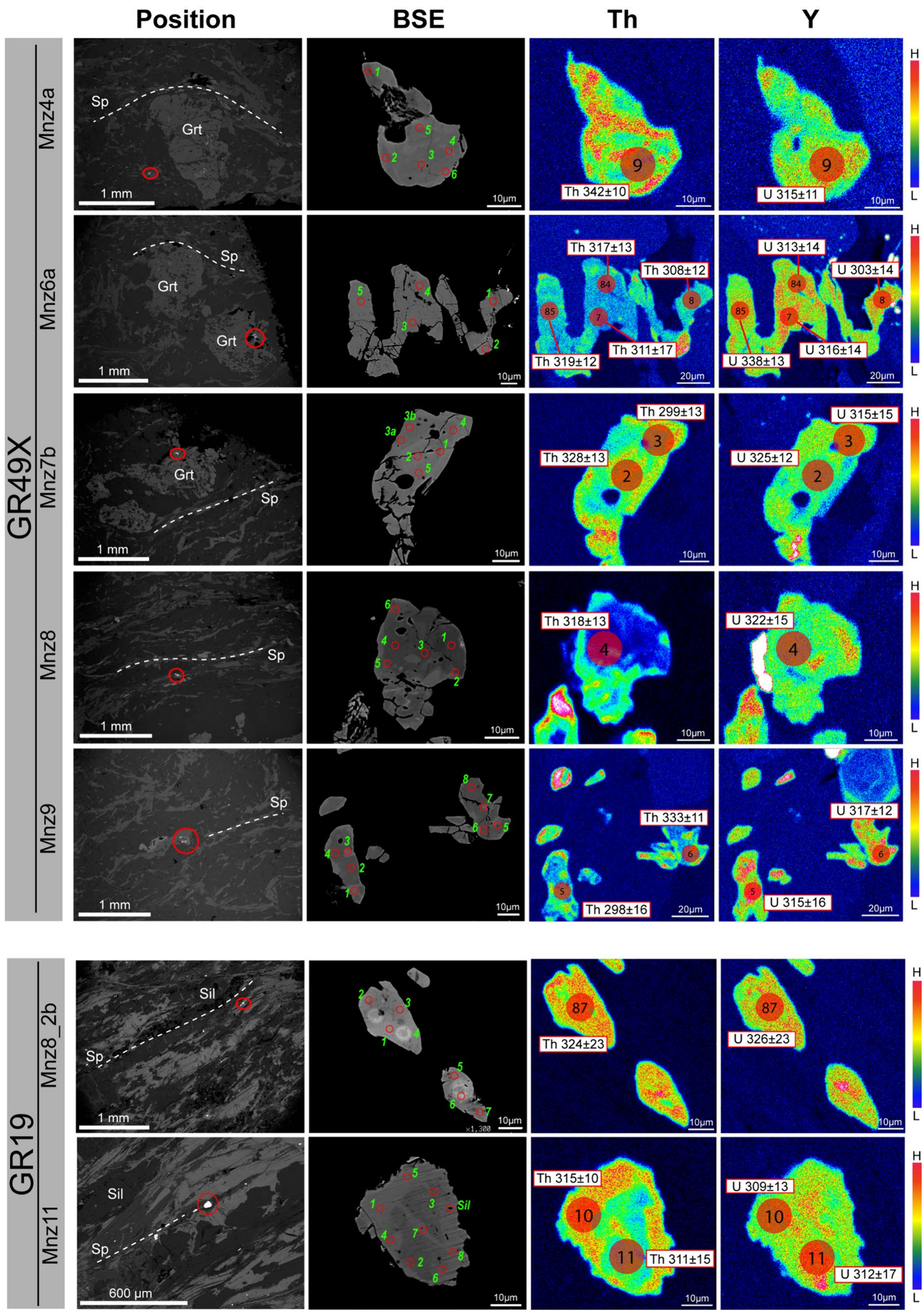
Position
BSE
Th
Y
GR49X
Mnz4a
Mnz6a
Mnz7b
Mnz8
Mnz9
GR19
Mnz8_2b
Mnz11
Sp
Grt
Sil
1 mm
600 µm
10µm
20µm
H
L
Th 342±10
U 315±11
Th 317±13
Th 308±12
Th 311±17
Th 319±12
U 313±14
U 303±14
U 316±14
U 338±13
Th 299±13
Th 328±13
U 315±15
U 325±12
Th 318±13
U 322±15
Th 333±11
Th 298±16
U 317±12
U 315±16
Th 324±23
U 326±23
Th 315±10
Th 311±15
U 309±13
U 312±17

Fig. 7 Textural position, back-scattered electron images and Th, Y chemical maps of selected monazites. Red dots represent the spots of quantitative chemical analyses. Compositional maps of Th and Y made by electron microprobe with spot location and the corresponding $^{208}Pb/^{232}Th$ (Th) and $^{206}Pb/^{238}U$ (U) ages are shown; color bar scale qualitatively points lower (L) to higher (H) Y–Th concentration

Results are similar for the two samples, with no variation in ages between different chemical domains within the analytical error.

Discussion

*P–T–*D*–t* tectono-metamorphic evolution

The combination of structural investigations at different scales (from meso- to microscale), with the *P–T* estimations from pseudosection (or forward) modelling integrated with conventional Ti-in-biotite geothermometry, have elucidated the tectono-metamorphic evolution of four ductile deformation phases in the study area. Correlations between the deformation phases identified in this work, indicated with the subscript "p" and those previously proposed in the area (Musumeci et al. 2015; Cruciani et al. 2016) are reported in Supplementary Material S5.

D_{p-1} structures are associated with a relict S_{p-1} foliation both in the hinges of F_p folds or as an internal foliation in porphyroblasts. The dominant structural architecture of the study area is controlled by the D_p phase, where the deformation is partitioned into low- and high-strain zones. Moving toward the MGSZ, strain increases progressively and is characterised by an increase in the degree of non-coaxial deformation. D_p folds become smaller and less frequent in the high-strain zones, while the mylonitic foliation becomes more penetrative and continuous (strain partitioning; e.g., Jones and Tanner 1995). Our data highlight, in agreement with previous authors (Columbu et al. 2015), an increase in strain and in the abundance of kinematic indicators towards the MGSZ, with mylonites observable in both the IC and the MGC. The mylonitic foliation in the MGSZ is from moderate to sub-vertical and the lineation is from gently plunging to sub-horizontal.

The kinematics of ductile D_p deformation in terms of the percentages of progressive pure and simple shear components were determined using two independent methods. Although different lithologies (i.e., gneiss vs micaschist) with different rheologies and possibly strain memory were analysed along the studied transects, our W_m estimates indicate that a strong component of pure shear was acting together with simple shear (Fossen and Tikoff 1998; 77–64% pure shear and 23–36% simple shear components, see Fig. 5). No significant variations between both methods and different lithologies were observed. In a classical pure shear dominated transpressional regime in which the extrusion component is upwards in the dip direction of the deformation zone, we should expect that the lineation should be sub-vertical or steeply plunging (Sanderson and Marchini 1984; Robin and Cruden 1994). However, in the case of a transpressive regime, models predict two end members with horizontal or vertical extrusion (Fossen and Tikoff 1998; Schulmann et al. 2003; Iacopini et al. 2008) depending on the orientation of the maximum axis of the finite strain ellipsoid. Iacopini et al. (2008) demonstrated that the orientation of the lineation is a function of time, strain rate and vorticity. Assuming constant strain rate, in the case of horizontal extrusion, Iacopini et al. (2008) demonstrated that a decrease in kinematic vorticity number increases the tendency of the lineation to develop sub-horizontally. In particular for low kinematic vorticity values, as in this case study, the lineation develops from gentle plunging to sub-horizontally and its orientation is stable in the flow during the progressive deformation (see Fig. 14 in Iacopini et al. 2008).

A possibility to explain the presence of sub-horizontal stretching lineations in a transpressional tectonic setting could be that at the beginning of the activation of the shear zone the pure shear component is predominant and a steeply plunging lineation develops and later, during progressive deformation, the (dextral) simple shear component increases which reorients the lineation to a sub-horizontal attitude.

We need also to consider that a deep seated shear zone such as the MGSZ developed under P conditions of 0.4–0.6 GPa and $T = 650$ °C, suggesting a crustal depth of nearly 12–18 km. In this case the expected vertical extrusion is not easy since it is counteracted by the lithostatic load. The sheared ductile material needs to escape but if the vertical movement is obstructed by the lithostatic pressure it will flow in another direction. A non planar dextral vertical strike slip shear zone, with dextral releasing bends could easily accommodate horizontal extrusion induced by the pure shear component. In addition, according to Iacopini et al. (2008) horizontal extrusion in a sub-vertical, ductile transpressional shear zone is theoretically possible and the horizontally extruded material can easily follow the space created by progressively opening releasing bends. This can also aid in the emplacement of the syn-kinematic leucogranite and tonalite magmas.

Another possibility to explain the structural setting could be the presence of overprinting tectonic events that in the present study could have involved thrusting followed by strike slip tectonics.

Nevertheless, the subvertical attitude of the mylonitic foliation in the MGSZ is compatible with a transpressive regime associated with a dextral shear deformation with a shortening component perpendicular to the shear zone boundaries. In the case of transtensional deformation, as

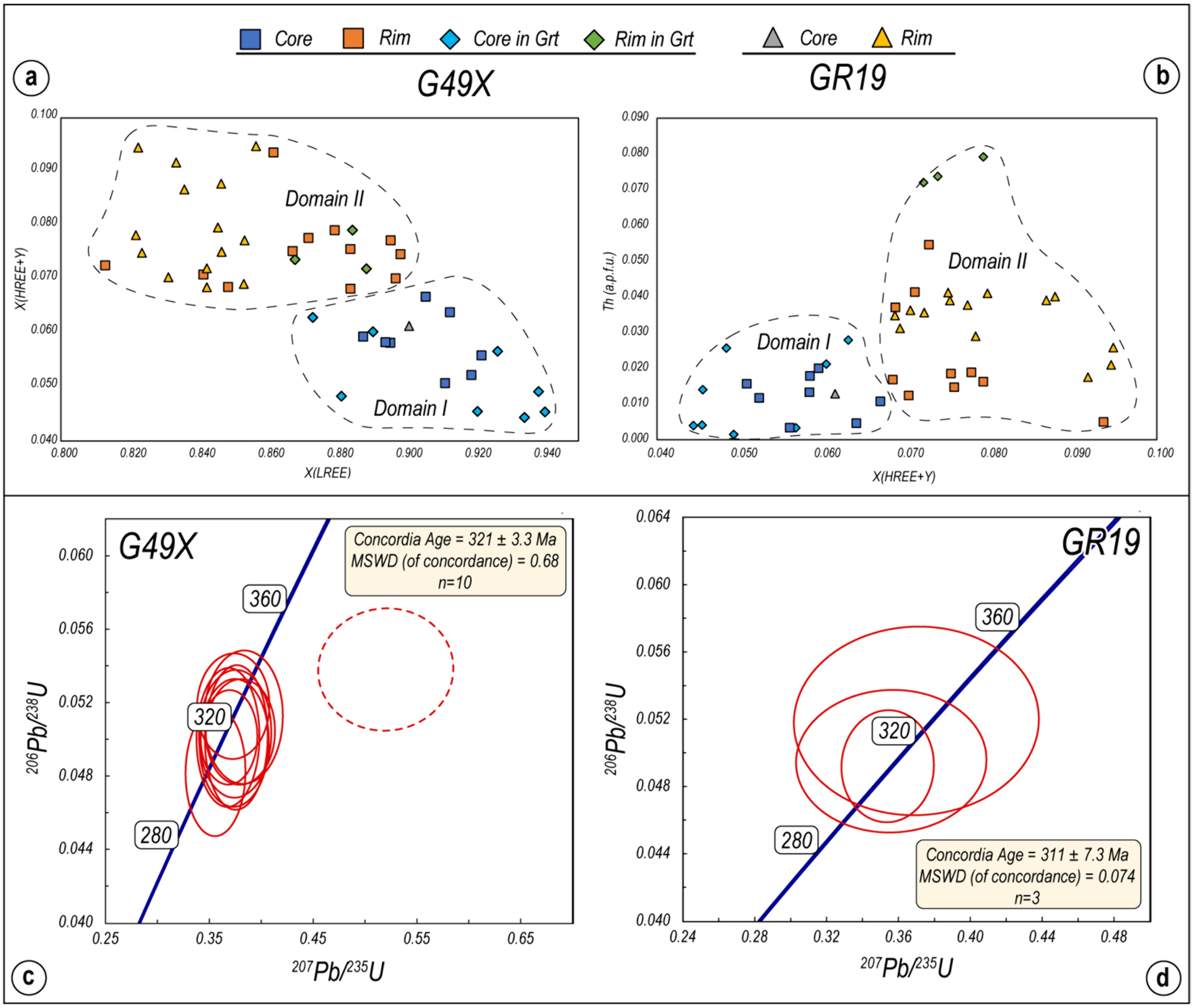

Fig. 8 Chemical monazite variations in sample G49X and GR19: **a** *X*(HREE + Y) vs. *X*(LREE) plot and in **b** *X*(Y + HREE) vs. Th plot. *X*(HREE + Y) is defined as (HREE + Y)/REE, whereas *X*(LREE) is LREE/REE. In both diagrams, monazite compositional domains (I and II) and the microstructural position of the analysed grains are highlighted; **c** and **d** $^{206}Pb/^{238}U$ versus $^{207}Pb/^{235}U$ concordia diagrams for sample G49X and GR19. In sample G49X the dashed ellipse indicates a spot not aligned along the concordia line

previously suggested by Musumeci (1992) and Cruciani et al. (2016), the attitude of the mylonitic foliation is expected to be sub-horizontal due to the main sub-vertical shortening direction (Fossen et al. 1994; Schulmann et al. 2003).

F_p and F_{p+1} fold axes show the same trend but not the same plunge angle. This could be associated with the ongoing deformation with a sub-horizontal or slightly inclined shortening up to the final stages of collisional events. Subsequent post-collision and post-transpression gravitational instability led to the development of open folds with shallowly dipping axial planes (F_{p+2}). This geometry suggests the gravitational collapse of a thickened orogen (Carmignani et al. 1994).

A NE to SW increase in metamorphic grade is observed, in agreement with Musumeci et al. (2015) and Cruciani et al. (2016). The syn-kinematic D_p mineral assemblage (sillimanite + biotite + white mica) parallel to the S_p mylonitic foliation is indicative of medium- to high-temperature amphibolite-facies conditions. Phase equilibrium modelling suggests peak *P–T* conditions at ~ 0.4–0.6 GPa and ~ 625 °C, pointing to a high-temperature and low-pressure (H*T*/L*P*) thermal regime. Taking into account the uncertainties in our *P–T* estimates and those of previous studies (Cruciani et al. 2016), the observed non-coaxial deformation could be associated with *P–T* conditions of ~ 625 ± 25 °C and ~ 0.4 ± 0.1 GPa. The investigated mylonitic sample clearly shows sillimanite oriented parallel to S_p, suggesting that ductile deformation was still active under high-temperature conditions when sillimanite was stable. The results obtained from the thermodynamic modelling are also supported by quartz microstructures and Ti-in-biotite temperatures (625 ± 25 °C). The growth of fibrolitic sillimanite at the expense of the prismatic grains, and the presence of post-S_p biotite, may represent growth on a retrograde path during the late stages of the transpression. These conditions are consistent with the retrograde path observed by Cruciani et al. (2016).

The timing of the D_p event has been constrained by in situ U–(Th)–Pb monazite dating. Even though some monazite compositional features differ between the samples, both record a similar and comparable timing on the S_p both inside and outside the high-strain zone. This is in agreement with deformation partitioning, where contemporaneous low- and high-strain zones occurred during D_p transpression. The obtained ages of ca. 315 Ma are associated with high-Y and low-Th inner rims and in monazites that grew along S_p. In addition, the monazite crystal with sillimanite inclusions (Sample GR19, Mnz 11), compatible with domain II of the monazite chemical group, indicates similar ages at ca. 315–310 Ma, constraining the age of non-coaxial deformation. Enhanced strain partitioning characterized by low- and high-strain zones could have favoured the emplacement of igneous intrusions along weak zones during the late stages of the non-coaxial deformation (Fig. 9a). This is consistent with the syn-tectonic emplacement age of the IC at ca. 305–295 Ma (Del Moro et al. 1991) within the MGSZ and the presence of sheared granites, which highlights that deformation linked to dextral transpression was still active until ca. 300 Ma. These data indicate that the MGSZ was active over a time span of ca. 15 Ma.

The MGSZ: implications for late-Carboniferous transpressive deformation

Late Variscan transpressive shear zones played a fundamental role in the architecture of the Sardinian Variscan belt (325–305 Ma, Di Vincenzo et al. 2004; Carosi et al. 2012, 2020; Cruciani et al. 2022a, b). Similar architecture to that documented here for the MGSZ has also been described in the northern sector of Sardinia, where the amphibolite-facies transpressive Posada-Asinara shear zone is exposed (PASZ; Carosi and Oggiano 2002; Carosi and Palmeri 2002; Iacopini et al. 2008; Frassi et al. 2009; Carosi et al. 2012, 2020, 2022; Graziani et al. 2020; Petroccia 2023). The amphibolite-facies metamorphic conditions recorded by both shear zones are highlighted by the presence of syn-kinematic sillimanite + biotite or biotite + white mica parallel to the mylonitic foliation. The PASZ developed under decreasing

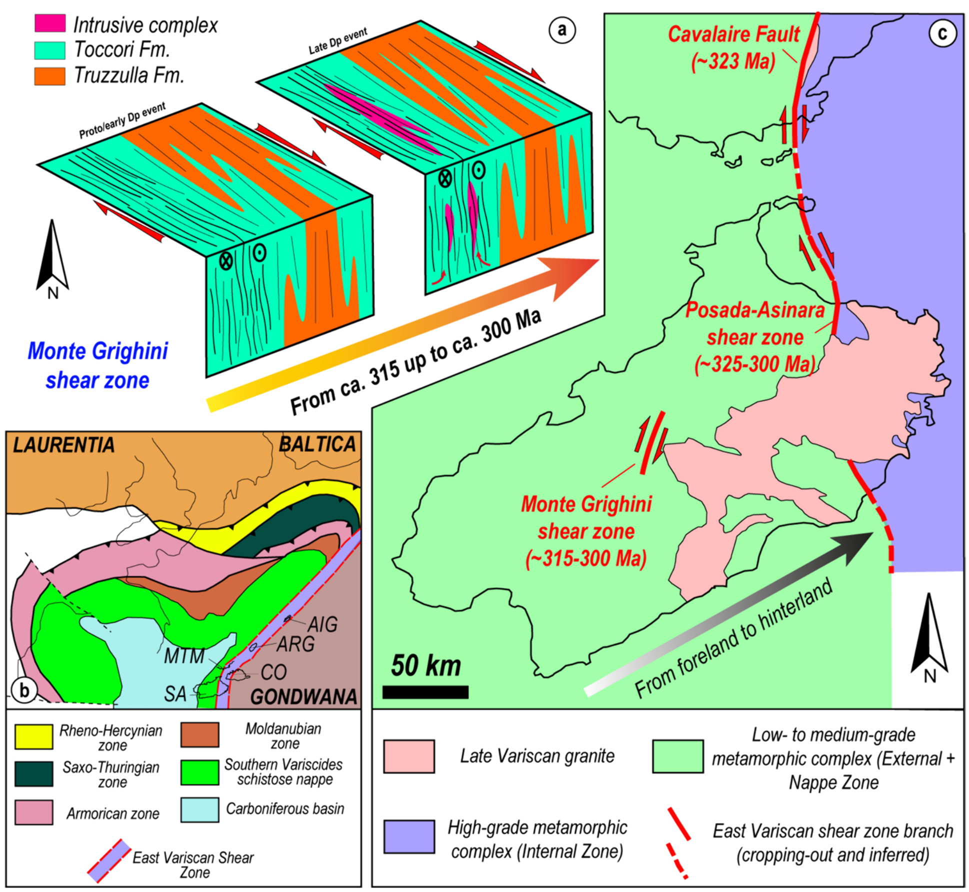

Fig. 9 **a** Simplified scheme of the tectonic evolution of MGSZ deduced from structural observations and the *P–T–t* results. The late syn-D_p intrusions have been provided; **b** Sketch maps of the Southern European Variscan belt during the late Carboniferous (modified from Corsini and Rolland 2009; *SA* Sardinia, *MTM* Maures–Tanneron Massif, *CO* Corsica, *ARG* Argentera Massif, *AIG* Aiguilles Rouge Massif); **c** Inferred lateral relationships between the branches of EVSZ during the late Carboniferous (modified after Simonetti et al. 2020a, b)

temperature and pressure, starting at ca. 325 Ma and was active for ca. 25 Ma. Carosi et al. (2020) constrained the timing of the activity of the PASZ using the same in situ monazite dating approach used in this work. The MGSZ and the PASZ record a similar percentage of pure shear deformation (Carosi et al. 2020; Petroccia 2023). Our new data enhances a possible correlation of the MGSZ to the PASZ in the Sardinian Variscan belt framework, already proposed by Elter et al. (1990).

Geochronological data indicate that similar ages for the onset of transpression in the MGSZ have been obtained in different sectors of the Southern European Variscan belt (Simonetti 2021; Carosi et al. 2022; Fig. 9b). In particular, similar features and ages of transpressive tectonics have been observed in Sardinia (Carosi et al. 2020), as well as in the Maures–Tanneron Massif (MTM, France; Simonetti et al. 2020a; Bolle et al. 2023) and in the External Crystalline Massif (Italy and France; Simonetti et al. 2018, 2020b, 2021; Jacob et al. 2021; Fréville et al. 2022; Vanardois et al. 2022a, b). All these have been associated with the East Variscan Shear Zone framework (EVSZ; Matte 2001; Corsini and Rolland 2009; Padovano et al. 2012, 2014; Simonetti 2021; Fig. 9b). The EVSZ is a network of interconnected transpressive shear zones displaying a similar evolution (Simonetti 2021). The oldest ages (ca. 340 Ma; Simonetti et al. 2018, 2021) of the transpressive deformation are found in the External Crystalline Massif, whereas within the MTM (ca. 323 Ma) and the island of Sardinia (ca. 325–300 Ma), ages are younger. The MGSZ is slightly younger (ca. 315–300 Ma) than the PASZ in Sardina (Fig. 8c). According to Simonetti et al. (2020b), it is therefore possible that transpressional deformation within the EVSZ preferentially started to be accommodated in the lower, migmatitic crust (External Crystalline Massif; Simonetti et al. 2021; Bühler et al. 2022; Vanardois et al. 2022a, b) and later shifted into the medium- and high-grade metamorphic complex, as in northern Sardinia and the MTM (Carosi et al. 2020, 2022; Simonetti et al. 2020a). Until now, transpressive shear linked to the EVSZ has only been recognised at the boundary between the medium- and the high-grade rocks or within the migmatitic complex. However, transpression in the MGSZ started later than in other, more internal, shear zones (e.g., the PASZ in Sardinia). This is possibly caused by the progressive migration and rejuvenation of deformation from the core or the hinterland to the external sectors of the collisional belt. Integrating our results with the existing findings, the tectonic framework of EVSZ represents a network of interconnected transpressive shear zones that, due to the progressive migration of the deformation over time, localized initially in the migmatitic crust, and later affected the medium- and high-grade metamorphic complex and finally the nappe zone located in the hinterland–foreland transition zone of the Variscan belt.

Conclusions

We carried out a geological investigation to elucidate the tectono-metamorphic evolution of the non-coaxial deformation linked to the MGSZ. This study has both local and regional implications for the interpretation of this shear zone within the Sardinian Variscan belt and its role in the late-Carboniferous Variscan orogeny. We have demonstrated the following:

1. Meso- and microstructural data highlight that the principal structures associated with the D_p formed during deformation in which strain was partitioned into low-strain zones mostly dominated by folding and high-strain zones dominated by LS tectonites and kinematic indicators. Kinematic analysis of ductile flow structures within the high-strain zone indicates non-coaxial deformation under a pure shear-dominated transpressive regime. Phase equilibrium modelling indicates that the formation of mylonitic fabrics within the MGSZ occurred under H*T*-L*P* amphibolite-facies conditions at ~ 625 °C and ~ 0.4–0.6 GPa.
2. In situ U–(Th)–Pb geochronology on monazite highlights the same age of the deformation within the low- and high-strain zones. The onset and the progressive evolution of the MGSZ with the associated syn-kinematic intrusions lasted from ca. 315 up to ca. 300 Ma, over a time span activity of ca. 15 Ma.
3. The MGSZ shows striking similarities with other dextral ductile transpressive shear zones within both the Sardinian Variscan chain (e.g., the PASZ) and other Variscan basements in Southern Europe. Owing to its position within the chain (i.e., hinterland–foreland transition zone or Nappe Zone) and the obtained ages, the MGSZ was one of the youngest and most external transpressive shear zones active in the EVSZ framework. Our data highlight that the network of interconnected transpressive shear zones related to the EVSZ also deformed, as in the MGSZ, the nappe zone of the Variscan belt.

Software

The map has been drawn using QGis3.16 Hannover, and its final assemblage has been realized with Adobe Illustrator® CC 2020. Structural data have been plotted with the software Stereonet© 10. The kinematic vorticity analysis with the stable porphyroclasts method and the finite strain analysis were performed using the software EllipseFit 3.2 by Vollmer (2015). Geochronological data were treated with Isoplot 3.70 (Ludwig 2008).

Supplementary Information The online version contains supplementary material available at https://doi.org/10.1007/s00531-024-02410-0.

Acknowledgements The research was supported by funds "Ricerca locale" (ex-60%), University of Torino (Montomoli C., Iaccarino S.). We thank the two reviewers, Elena Druguet, Samuele Papeschi and topic editor Alexander Cruden for their comments that improved the original manuscript. The editor, Ulrich Riller, is thanked for his careful editorial work and suggestions. We thank Marcello Franceschelli and Gabriele Cruciani for fruitfull discussion. This paper is based on the first author (A.P.) PhD project under the supervision of R.C., C.M. and S.I.

Funding Open access funding provided by Università degli Studi di Torino within the CRUI-CARE Agreement.

Data availability The authors declare that all data supporting the findings of this study are available within the article.

Declarations

Conflict of interest All the authors declare that they have no conflict of interest.

References

Aguilar C, Liesa M, Štípská P, Schulmann K, Muñoz JA, Casas JM (2015) P–T–t–d evolution of orogenic middle crust of the Roc de Frausa Massif (Eastern Pyrenees): a result of horizontal crustal flow and Carboniferous doming? J Metamorph Geol 33(3):273–294. https://doi.org/10.1111/jmg.12120

Aleinikoff JN, Schenck WS, Plank MO, Srogi L, Fanning CM, Kamo SL, Bosbyshell H (2006) Deciphering igneous and metamorphic events in high-grade rocks of the Wilmington Complex, Delaware: morphology, cathodoluminescence and backscattered electron zoning, and SHRIMP U−Pb geochronology of zircon and monazite. Geol Soc Am Bull 118(1–2):39–64. https://doi.org/10.1130/B25659.1

Arthaud F, Matte P (1977) Late Paleozoic strike-slip faulting in southern Europe and northern Africa: result of a right-lateral shear zone between the Appalachians and the Urals. Geol Soc Am Bull 88(9):1305–1320. https://doi.org/10.1130/0016-7606(1977)88%3C1305:LPSFIS%3E2.0.CO;2

Barca S, Forci A, Funedda A (2003) Nuovi dati stratigrafico-strutturali sul flysch ercinico dell'Unità del Gerrei (Sardegna SE). In: Pascucci V (ed) GeoSed, Alghero 28–30 settembre 2003. University of Sassari, Sassari, pp 291–298

Bolle O, Corsini M, Diot H, Laurent O, Melis R (2023) Late-orogenic evolution of the Southern European Variscan Belt constrained by fabric analysis and dating of the Camarat Granitic Complex and coeval felsic dykes (Maures–Tanneron Massif, SE France). Tectonics. https://doi.org/10.1029/2022TC007310

Broussolle A, Štípská P, Lehmann J, Schulmann K, Hacker BR, Holder R, Kylander-Clark ARC, Hanžl P, Racek M, Hasalová P, Lexa O, Hrdličková K, Buriánek D (2015) P–T–t–D record of crustal-scale horizontal flow and magma-assisted doming in the SW Mongolian Altai. J Metamorph Geol 33:359–383. https://doi.org/10.1111/jmg.12124

Bühler M, Zurbriggen R, Berger A, Herwegh M, Rubatto D (2022) Late Carboniferous Schlingen in the Gotthard nappe (Central Alps) and their relation to the Variscan evolution. Int J Earth Sci. https://doi.org/10.1007/s00531-022-02247-5

Burg JP, Kaus BJ, Podladchikov YY (2004) Dome structures in collision orogens: mechanical investigation of the gravity/compression interplay. Geol S Am S. https://doi.org/10.1130/0-8137-2380-9.47

Cao S, Zhan L, Tao L (2022) Exhumation processes of continental crustal metamorphic complexes. GeoGeo. https://doi.org/10.1016/j.geogeo.2022.100094

Carmignani L, Pertusati PC (1977) Analisi strutturale di un segmento della catena ercinica: il Gerrei (Sardegna sud-orientale). Bull Soc Geol Ital 96:339–364

Carmignani L, Minzoni N, Pertusati PC, Gattiglio M (1982) Lineamenti geologici principali del Sarcidano-Barbagia di Belvì. In: Carmignani L, Cocozza T, Ghezzo C, Pertusati PC, Ricci CA (eds) Guida alla Geologia del Paleozoico Sardo. Guide Geologiche Regionali, Società Geologica Italiana, pp 119–125

Carmignani L, Cherchi GP, Franceschelli M, Ghezzo C, Musumeci G, Pertusati PC (1987) The mylonitic granitoids and tectonic Units of the Monte Grighini Complex (West-Central Sardinia): a preliminary note. In: Paleozoic stratgraphy, tectonics and magmatism in Italy, pp 25–26.

Carmignani L, Carosi R, Di Pisa A, Gattiglio M, Musumeci G, Oggiano G, Pertusati PC (1994) The hercynian chain in Sardinia (Italy). Geodin Acta 7(1):31–47. https://doi.org/10.1080/09853111.1994.11105257

Carmignani L, Oggiano G, Barca S, Conti P, Eltrudis A, Funedda A, Pasci S, Salvadori I (2001) Geologia della Sardegna (Note illustrative della Carta Geologica della Sardegna in scala 1:200.000). Memorie descrittive della Carta Geologica d'Italia, Servizio Geologico Nazionale, Istituto Poligrafico e Zecca dello Stato, Roma

Carmignani L, Conti P, Funedda A, Oggiano G, Pasci S (2012) La geologia della Sardegna-84 Congresso Nazionale della Società Geologica Italiana. In: Geology of Sardinia–84 national conference of the Italian Geological Society

Carmignani L, Oggiano G, Funedda A, Conti P, Pasci S (2015) The geological map of Sardinia (Italy) at 1:250,000 scale. J Maps 12(5):826–835. https://doi.org/10.1080/17445647.2015.1084544

Carosi R, Malfatti G (1995) Analisi Strutturale dell'Unità di Meana Sardo e caratteri della deformazione duttile nel Sarcidano-Barbagia di Seulo (Sardegna centrale, Italia). Atti Soc. Toscana Sci Nat Mem A 102:121–136

Carosi R, Oggiano G (2002) Transpressional deformation in northwestern Sardinia (Italy): insights on the tectonic evolution of the Variscan belt. Cr Geosci 334(4):287–294. https://doi.org/10.1016/S1631-0713(02)01740-6

Carosi R, Palmeri R (2002) Orogen-parallel tectonic transport in the Variscan belt of northeastern Sardinia (Italy): implications for the exhumation of medium-pressure metamorphic rocks. Geol Mag 139(5):497–511. https://doi.org/10.1017/S0016756802006763

Carosi R, Pertusati PC (1990) Evoluzione strutturale delle unità tettoniche erciniche nella Sardegna centro-meridionale. Bull Soc Geol Ital 109:325–335

Carosi R, Musumeci G, Pertusati PC (1991) Differences in the structural evolution of tectonic units in central-southern Sardinia. Bull Soc Geol Ital 110(3–4):543–551

Carosi R, Montomoli C, Iacopini D (2002) Le pieghe asimmetriche dell'Unità di Meana Sardo, Sardegna centrale (Italia): evoluzione e meccanismi di piegamento. Atti Soc Toscana Sci Nat Mem A 108:51–58

Carosi R, Iacopini D, Montomoli C (2004) Asymmetric folds development in the Variscan Nappe of central Sardinia (Italy). Cr Geosci 336(10):939–949. https://doi.org/10.1016/j.crte.2004.03.004

Carosi R, Leoni L, Paolucci Z, Pertusati PC, Trumpy E (2010) Deformation and illite crystallinity in metapelitic rocks from the Mandas area, in the Nappe Zone of the Variscan belt of Sardinia. Rendiconti Online Società Geologica Italiana 11:393–394

Carosi R, Montomoli C, Tiepolo M, Frassi C (2012) Geochronological constraints on post-collisional shear zones in the Variscides of Sardinia (Italy). Terra Nova 24(1):42–51. https://doi.org/10.1111/j.1365-3121.2011.01035.x

Carosi R, Petroccia A, Iaccarino S, Simonetti M, Langone A, Montomoli C (2020) Kinematics and timing constraints in a transpressive tectonic regime: the example of the Posada-Asinara shear zone (NE Sardinia, Italy). Geosciences 10:288. https://doi.org/10.3390/geosciences10080288

Carosi R, Montomoli C, Iaccarino S, Benetti B, Petroccia A, Simonetti M (2022) Constraining the timing of evolution of shear zones in two collisional orogens: fusing structural geology and geochronology. Geosciences 12:231. https://doi.org/10.3390/geosciences12060231

Carreras J, Druguet E (2014) Framing the tectonic regime of the NE Iberian Variscan segment. Geol Soc Lond Spec Publ 405(1):249–264. https://doi.org/10.1144/SP405.7

Chen SY, Zhang B, Zhang JJ, Wang Y, Li XR, Zhang L, Yan Y, Cai F, Yue Y (2022) Tectonic transformation from orogen-perpendicular to orogen-parallel extension in the North Himalayan Gneiss Domes: Evidence from a structural, kinematic, and geochronological investigation of the Ramba gneiss dome. J Struct Geol 155:104527. https://doi.org/10.1016/j.jsg.2022.104527

Chew DM, Petrus JA, Kamber BS (2014) U-Pb LA–ICPMS dating using accessory mineral standards with variable common Pb. Chem Geol 363:185–199. https://doi.org/10.1016/j.chemgeo.2013.11.006

Cocco F, Oggiano G, Funedda A, Loi A, Casini L (2018) Stratigraphic, magmatic and structural features of Ordovician tectonics in Sardinia (Italy): a review. J Iber Geol 44:619–639. https://doi.org/10.1007/s41513-018-0075-1

Cocco F, Loi A, Funedda A, Casini L, Ghienne JF, Pillola GL, Vidal M, Meloni MA, Oggiano G (2022) Ordovician tectonics of the South European Variscan Realm: new insights from Sardinia. Int J Eart Sci. https://doi.org/10.1007/s00531-022-02250-w

Cochelin B, Lemirre B, Denèle Y, de Saint Blanquat M (2021) Strain partitioning within bending orogens, new insights from the Variscan belt (Chiroulet-Lesponne domes, Pyrenees). Tectonics. https://doi.org/10.1029/2020TC006386

Columbu S, Cruciani G, Fancello D, Franceschelli M, Musumeci G (2015) Petrophysical properties of a granite-protomylonite-ultramylonite sequence: insight from the Monte Grighini shear zone, central Sardinia. Italy Eur J Mineral 27(4):471–486. https://doi.org/10.1127/ejm/2015/0027-2447

Coney PJ, Harms TA (1984) Cordilleran metamorphic core complexes: Cenozoic extensional relics of Mesozoic compression. Geology 12(9):550–554. https://doi.org/10.1130/0091-7613(1984)12%3C550:CMCCCE%3E2.0.CO;2

Coney PJ, Crittenden MD, Davis GH (1980) Cordilleran metamorphic core complexes: an overview. Cordilleran metamorphic core complexes. Geol Soc Am Mem 153:7–31

Conti P, Funedda A, Cerbai N (1998) Mylonite development in the Hercynian basement of Sardinia (Italy). J Struct Geol 20(2/3):121–133. https://doi.org/10.1016/S0191-8141(97)00091-6

Conti P, Carmignani L, Cerbai N, Eltrudis A, Funedda A, Oggiano G (1999) From thickening to extension in the Variscan belt - kinematic evidence from Sardinia (Italy). Terra Nova 11(2/3):93–99. https://doi.org/10.1046/j.1365-3121.1999.00231.x

Conti P, Carmignani L, Funedda A (2001) Change of nappe transport direction during the Variscan collisional evolution of central-southern Sardinia (Italy). Tectonophysics 332(1–2):255–273. https://doi.org/10.1016/S0040-1951(00)00260-2

Corsini M, Rolland Y (2009) Late evolution of the southern European Variscan belt: exhumation of the lower crust in a context of oblique convergence. Cr Geosci 341(2–3):214–223. https://doi.org/10.1016/j.crte.2008.12.002

Cruciani G, Franceschelli M, Musumeci G, Spano ME, Tiepolo M (2013) U−Pb zircon dating and nature of metavolcanics and metarkoses from the Monte Grighini Unit: new insights on Late Ordovician magmatism in the Variscan belt in Sardinia, Italy. Int J Earth Sci 102:2077–2096. https://doi.org/10.1007/s00531-013-0919-z

Cruciani G, Montomoli C, Carosi R, Franceschelli M, Puxeddu M (2015) Continental collision from two perspectives: a review of Variscan metamorphism and deformation in northern Sardinia. Period Mineral 84:657–699. https://doi.org/10.2451/2015PM0455

Cruciani G, Franceschelli M, Massonne HJ, Musumeci G, Spano ME (2016) Thermomechanical evolution of the highgrade core in the nappe zone of Variscan Sardinia, Italy: the role of shear deformation and granite emplacement. J Metamorph Geol 34:321–342. https://doi.org/10.1111/jmg.12183

Cruciani G, Fancello D, Franceschelli M, Giovanni M (2017) The Paleozoic basement of Monte Grighini Unit, a deep view in the nappe structure of Variscan belt in Sardinia. Synthesis of geological data and field guide. Atti Della Societa Toscana Di Scienze Naturali. https://doi.org/10.2424/ASTSN.M.2017.19

Cruciani G, Dulcetta L, Franceschelli M, Frassi C, Musumeci G (2022a) Hot metamorphic complex in the Foreland Zone of the Variscan chain: insights from the Monte Filau orthogneiss (SW Sardinia). Italy Ital J Geosci 141(3):385–399. https://doi.org/10.3301/IJG.2022.22

Cruciani G, Franceschelli M, Carosi R, Montomoli C (2022b) P−T path from garnet zoning in pelitic schist from NE Sardinia, Italy: further constraints on the metamorphic and tectonic evolution of the north Sardinia Variscan belt. Lithos. https://doi.org/10.1016/j.lithos.2022.106836

De Capitani C, Brown TH (1987) The computation of chemical equilibrium in complex systems containing non-ideal solutions. Geochim Cosmochim Ac 51:2639–2652. https://doi.org/10.1016/0016-7037(87)90145-1

De Capitani C, Petrakakis K (2010) The computation of equilibrium assemblage diagrams with Theriak/Domino software. Am Mineral 95:1006–1016. https://doi.org/10.2138/am.2010.3354

Del Moro A, Laurenzi M, Musumeci G, Pardini G (1991) Rb/Sr and Ar/Ar chronology of Hercynian Mt. Grighini intrusive and metamorphic rocks (central-western Sardinia). Plinius 4:121–122

Denèle Y, Olivier P, Gleizes G, Barbey P (2007) The Hospitalet gneiss dome (Pyrenees) revisited: lateral flow during Variscan transpression in the middle crust. Terra Nova 19:445–453. https://doi.org/10.1111/j.1365-3121.2007.00770.x

Denèle Y, Olivier Ph, Gleizes G, Barbey P (2009) Decoupling between the middle and upper crust during transpression-related lateral flow: Variscan evolution of the Aston gneiss dome (Pyrenees, France). Tectonophysics 477:244–261. https://doi.org/10.1016/j.tecto.2009.04.033

Di Vincenzo G, Carosi R, Palmeri R (2004) The relationship between tectono-metamorphic evolution and argon isotope records in white mica: constraints from in situ ^{40}Ar-^{39}Ar laser analysis of the Variscan basement of Sardinia. J Petrol 45:101–1043. https://doi.org/10.1093/petrology/egh002

Díaz-Azpiroz M, Barcos L, Balanyá JC, Fernández C, Expósito I, Czeck DM (2014) Applying a general triclinic transpression model to highly partitioned brittle-ductile shear zones: a case study from the Torcal de Antequera massif, external Betics, southern Spain. J Struct Geol 68:316–336. https://doi.org/10.1016/j.jsg.2014.05.010

Druguet E (2001) Development of high thermal gradients by coeval transpression and magmatism during the Variscan orogen: insights from the Cap de Creus (Eastern Pyrenees). Bulletin De La Société Géologique De France 174:585–594

Dutton BJ (1997) Finite strains in transpression zones with no boundary slip. J Struct Geol 19(9):1189–1200. https://doi.org/10.1016/S0191-8141(97)00043-6

Elter FM, Musumeci G, Pertusati PC (1990) Late Hercynian shear zones in Sardinia. Tectonophysics 176(3–4):387–404. https://doi.org/10.1016/0040-1951(90)90080-R

Faure M, Lardeaux JM, Ledru P (2009) A review of the pre-Permian geology of the Variscan French Massif Central. Cr Geosci 341(2–3):202–213. https://doi.org/10.1016/j.crte.2008.12.001

Fitton JG, Gill RCO (1970) The oxidation of ferrous iron in rocks during mechanical grinding. Geochim Cosmochim Acta 34(4):518–524. https://doi.org/10.1016/0016-7037(70)90143-2

Forshaw JB, Pattison DR (2021) Ferrous/ferric (Fe^{2+}/Fe^{3+}) partitioning among silicates in metapelites. Contrib Mineral Petrol 176(9):63. https://doi.org/10.1007/s00410-021-01814-4

Forshaw JB, Pattison DR (2023) Major-element geochemistry of pelites. Geology 51(1):39–43. https://doi.org/10.1130/G50542.1

Forshaw JB, Waters DJ, Pattison DR, Palin RM, Gopon P (2019) A comparison of observed and thermodynamically predicted phase equilibria and mineral compositions in mafic granulites. J Metamorph Geol 37(2):153–179. https://doi.org/10.1111/jmg.12454

Forte AM, Bailey CM (2007) Testing the utility of the porphyroclast hyperbolic distribution method of kinematic vorticity analysis. J Struct Geol 29(6):983–1001. https://doi.org/10.1016/j.jsg.2007.01.006

Fossen H, Cavalcante GCG (2017) Shear zones—a review. Earth Sci Rev 171:434–455. https://doi.org/10.1016/j.earscirev.2017.05.002

Fossen H, Tikoff B (1993) The deformation matrix for simultaneous simple shearing, pure shearing and volume change, and its application to transpression-transtension tectonics. J Struct Geol 15:413–422. https://doi.org/10.1016/0191-8141(93)90137-Y

Fossen H, Tikoff B (1998) Extended models of transpression and transtension, and application to tectonic settings. Geol Soc Spec Publ 135(1):15–33. https://doi.org/10.1144/GSL.SP.1998.135.01.02

Fossen H, Tikoff B, Teyssier C (1994) Strain modeling of transpressional and transtensional deformation. Nor Geol Tidsskr 74(3):134–145

Fossen H, Teyssier C, Whitney D (2013) Transtensional folding. J Struct Geol 56(2013):89–102. https://doi.org/10.1016/j.jsg.2013.09.004

Franceschelli M, Gattiglio M, Pannuti F, Fadda S (1992) Illite crystallinity in pelitic rocks from the external and nappe zones of the Hercynian chain of Sardinia. In: Carmignani L, Sassi FP (eds) Contributions to the Geology of Italy with special regard to the Paleozoic Basements. IGCP Project No. 276, Newsletter, pp 127–135

Franke W, Żelaźniewicz A (2023) Variscan Evolution of the Bohemian Massif (Central Europe): fiction, facts and problems. Gondwana Res. https://doi.org/10.1016/j.gr.2023.06.012

Franke W, Cocks LRM, Torsvik TH (2017) The palaeozoic variscan oceans revisited. Gondwana Res 48:257–284. https://doi.org/10.1016/j.gr.2017.03.005

Frassi C, Carosi R, Montomoli C, Law RD (2009) Kinematics and vorticity of flow associated with post-collisional oblique transpression in the Variscan Axial Zone of northern Sardinia (Italy). J Struct Geol 31:1458–1471. https://doi.org/10.1016/j.jsg.2009.10.001

Fréville K, Trap P, Vanardois J, Melleton J, Faure M, Bruguier O, Poujol M, Lach P (2022) Carboniferous-Permian tectono-metamorphic evolution of the Pelvoux Massif (External Crystalline Massif, Western Alps), with discussion on flow kinematics of the Eastern-Variscan Shear Zone. BSGF Earth Sci Bull 193:13. https://doi.org/10.1051/bsgf/2022008

Fu J, Li G, Wang G, Zhang L, Liang W, Zhang X, Jiao Y, Dong S (2022) Structural and kinematic analysis of the Cuonadong dome, southern Tibet, China: Implications for middle-crust deformation. J Asian Earth Sci X 8:100112. https://doi.org/10.1016/j.jaesx.2022.100112

Funedda A, Naitza S, Conti P, Dini A, Buttau C, Tocco S (2011) The geological and metallogenic map of the Baccu Locci mine area (Sardinia, Italy). J Maps 7(1):103–114. https://doi.org/10.4113/jom.2011.1134

Funedda A, Meloni MA, Loi A (2015) Geology of the Variscan basement of the Laconi-Asuni area (central Sardinia, Italy): the core of a regional antiform refolding a tectonic nappe stack. J Maps 11(1):146–156. https://doi.org/10.1080/17445647.2014.942396

Gapais D, Brun JP, Gumiaux C, Cagnard F, Ruffet G, Le Carlier De Veslud C (2015) Extensional tectonics in the Hercynian Armorican belt (France). An overview. Bulletin De La Société Géologique De France 186(2–3):117–129. https://doi.org/10.2113/gssgfbull.186.2-3.117

Gébelin A, Roger F, Brunel M (2009) Syntectonic crustal melting and high-grade metamorphism in a transpressional regime, Variscan Massif Central, France. Tectonophysics 477(3–4):229–243. https://doi.org/10.1016/j.tecto.2009.03.022

Gillam BG, Little TA, Smith E, Toy VG (2013) Extensional shear band development on the outer margin of the Alpine mylonite zone, Tatare Stream, Southern Alps, New Zealand. J Struct Geol 54:1–20. https://doi.org/10.1016/j.jsg.2013.06.010

Gonçalves GO, Lana C, Scholz R, Buick IS, Gerdes A, Kamo SL, Corfu F, Marinho MM, Chaves AO, Valeriano C, Nalini HA (2016) An assessment of monazite from the Itamb´e pegmatite district for use as U−Pb isotope reference material for microanalysis and implications for the origin of the "Moacyr" monazite. Chem Geol 424:30–50. https://doi.org/10.1016/j.chemgeo.2015.12.019

Graziani R, Montomoli C, Iaccarino S, Menegon L, Nania L, Carosi R (2020) Structural setting of a transpressive shear zone: Insights from geological mapping, quartz petrofabric and kinematic vorticity analysis in NE Sardinia (Italy). Geol Mag. https://doi.org/10.1017//S0016756820000138

Henry DJ, Guidotti CV, Thomson JA (2005) The Ti-saturation surface for low-to-medium pressure metapelitic biotites: implications for geothermometry and Ti-substitution mechanisms. Am Mineral 90(2–3):316–328. https://doi.org/10.2138/am.2005.1498

Holland TJB, Powell R (2011) An improved and extended internally consistent thermodynamic dataset for phases of petrological interest, involving a new equation of state for solids. J Metamorph Geol 29(3):333–383. https://doi.org/10.1111/j.1525-1314.2010.00923.x

Holland TJB, Green ECR, Powell R (2021) A thermodynamic model for feldspars in $KAlSi_3O_8$−$NaAlSi_3O_8$−$CaAl_2Si_2O_8$ for mineral equilibrium calculations. J Metamorph Geol 40(4):587–600. https://doi.org/10.1111/jmg.12639

Horstwood MSA, Foster GL, Parrish RR, Noble SR, Nowell GM (2003) Common-Pb corrected in situ U–Pb accessory mineral geochronology by LA-MC-ICP-MS. J Anal Atom Spectrom 18:837–846. https://doi.org/10.1039/b304365g

Iacopini D, Carosi R, Montomoli C, Passchier CW (2008) Strain analysis and vorticity of flow in the Northern Sardinian Variscan Belt: recognition of a partitioned oblique deformation event. Tectonophysics 446(1–4):77–96. https://doi.org/10.1016/j.tecto.2007.10.002

Iacopini D, Frassi C, Carosi R, Montomoli C (2011) Biases in three-dimensional vorticity analysis using porphyroclast system: limits and application to natural examples. Geol Soc Spec Publ 360(1):301–318. https://doi.org/10.1144/SP360.17

Jacob JB, Guillot S, Rubatto D, Janots E, Melleton J, Faure M (2021) Carboniferous high-P metamorphism and deformation in the Belledonne Massif (Western Alps). J Metamorph Geol 39(8):1009–1044. https://doi.org/10.1111/jmg.12600

Jeffery GB (1922) The motion of ellipsoidal particles immersed in a viscous fluid. Proc R Soc Lond Ser A 102(715):161–179. https://doi.org/10.1098/rspa.1922.0078

Jessup MJ, Law RJ, Frassi C (2007) The Rigid Grain Net (RGN): An alternative method for estimating mean kinematic vorticity number (Wm). J Struct Geol 29:411–421. https://doi.org/10.1016/j.jsg.2006.11.003

Jones RR, Tanner PW (1995) Strain partitioning in transpression zones. J Struct Geol 17:793–802. https://doi.org/10.1016/0191-8141(94)00102-6

Jones RR, Holdsworth RE, Clegg P, McCaffrey K, Tavarnelli E (2004) Inclined transpression. J Struct Geol 26(8):1531–1548. https://doi.org/10.1016/j.jsg.2004.01.004

Kohn MJ, Engi M, Lanari P (2017) Petrochronology: methods and applications, vol 83. De Gruyter, Berlin. https://doi.org/10.1515/9783110561890

Kurz GA, Northrup CJ (2008) Structural analysis of mylonitic rocks in the Cougar Creek Complex, Oregon-Idaho using the porphyroclast hyperbolic distribution method, and potential use of SC′-type extensional shear bands as quantitative vorticity indicators. J Struct Geol 30(8):1005–1012. https://doi.org/10.1016/j.jsg.2008.04.003

Lanari P, Engi M (2017) Local bulk composition effects on metamorphic mineral assemblages. Rev Mineral Geochem 83(1):55–102. https://doi.org/10.2138/rmg.2017.83.3

Lanari P, Hermann J (2021) Iterative thermodynamic modelling—part 2: tracing equilibrium relationships between minerals in metamorphic rocks. J Metamorph Geol 39(6):651–674. https://doi.org/10.1111/jmg.12575

Lanari P, Vidal O, De Andrade V, Dubacq B, Lewin E, Grosch EG, Schwartz S (2014) XMapTools: A MATLAB©-based program for electron microprobe X-ray image processing and geothermobarometry. Comput Geosci 62:227–240. https://doi.org/10.1016/j.cageo.2013.08.010

Law RD (2014) Deformation thermometry based on quartz c-axis fabrics and recrystallisation microstructures: a review. J Struct Geol 66:129–161. https://doi.org/10.1016/j.jsg.2014.05.023

Law RD, Searle MP, Simpson RL (2004) Strain, deformation temperatures and vorticity of flow at the top of the Greater Himalayan Slab, Everest Massif. Tibet J Geol Soc London 161:305–320. https://doi.org/10.1144/0016-764903-047

Lister GS, Davis GA (1989) The origin of metamorphic core complexes and detachment faults formed during Tertiary continental extension in the northern Colorado River region, USA. J Struct Geol 11(1–2):65–94. https://doi.org/10.1016/0191-8141(89)90036-9

Loi A, Barca S, Chauvell JJ, Dabard MP, Leone F (1992) The Punta Sepeddì Formation near Dolianova (Sarrabus—SE Sardinia) recent petrographical and geochemical data. In: Carmignani L, Sassi FP (eds) Contribution to the Geology of Italy with special regard to the Paleozoic basement. A volume dedicated to Tommaso Cocozza, Vol. 5. Newsletter. Siena: IGCP Project No. 276, pp 163–166

Loi A, Cocco F, Oggiano G, Funedda A, Vidal M, Ferretti A, Leone F, Barca S, Naitza S, Ghienne JF, Pillola GL (2023) The Ordovician of Sardinia (Italy): from the "Sardic Phase" to the end-Ordovician glaciation, palaeogeography and geodynamic context. Geol Soc Spec Publ 532(1):409–431. https://doi.org/10.1144/SP532-2022-121

Ludwig KR (2003) Isoplot/Ex version 3.00: a geochronological toolkit for Microsoft Excel. Berkeley Geochronology Center, Berkeley

Matte P (2001) The Variscan collage and orogeny (480–290 Ma) and the tectonic definition of the Armorica microplate: a review. Terra Nova 13:117–121. https://doi.org/10.1046/j.1365-3121.2001.00327.x

Montel JM, Razafimahatratra D, de Parseval P, Poitrasson F, Moine B, Seydoux-Guillaume AM, Pik R, Arnaud N, Gibert F (2018) The giant monazite crystals from Manangotry (Madagascar). Chem Geol 484:36–50. https://doi.org/10.1016/j.chemgeo.2017.10.034

Montomoli C, Iaccarino S, Simonetti M, Lezzerini M, Carosi R (2018) Structural setting, kinematics and metamorphism in a km-scale shear zone in the inner nappes of Sardinia (Italy). Ital J Geosci 137:294–310. https://doi.org/10.3301/IJG.2018.16

Musumeci G (1992) Ductile wrench tectonics and exhumation of hercynian metamorphic basement in Sardinia: Monte Grighini Complex. Geodinam Act 5(1–2):119–133. https://doi.org/10.1080/09853111.1992.11105223

Musumeci G, Spano ME, Cherchi GP, Franceschelli M, Pertusati PC, Cruciani G (2015) Geological map of the Monte Grighini Variscan Complex (Sardinia, Italy). J Maps 11(2):287–298. https://doi.org/10.1080/17445647.2014.924441

Nabavi S, Alavi SA, Díaz-Azpiroz M, Mohammadi S, Ghassemi MR, Fernández C, Frehner M (2020) Deformation mechanics in inclined, brittle-ductile transpression zones: Insights from 3D finite element modelling. J Struct Geol 137:104082. https://doi.org/10.1016/j.jsg.2020.104082

Padovano M, Elter FM, Pandeli E, Franceschelli M (2012) The East Variscan Shear Zone: new insights into its role in the Late Carboniferous collision in southern Europe. Int Geol Rev 54(8):957–970. https://doi.org/10.1080/00206814.2011.626120

Padovano M, Dörr W, Elter FM, Gerdes A (2014) The east Variscan shear zone: geochronological constraints from the Capo Ferro area (NE Sardinia, Italy). Lithos 196:27–41. https://doi.org/10.1016/j.lithos.2014.01.015

Palin RM, Weller OM, Waters DJ, Dyck B (2016) Quantifying geological uncertainty in metamorphic phase equilibria modelling; a Monte Carlo assessment and implications for tectonic interpretations. GSF 7(4):591–607. https://doi.org/10.1016/j.gsf.2015.08.005

Passchier CW (1987) Stable positions of rigid objects in non-coaxial flow—a study in vorticity analysis. J Struct Geol 9(5–6):679–690. https://doi.org/10.1016/0191-8141(87)90152-0

Passchier CW (1998) Monoclinic model shear zones. J Struct Geol 20:1121–1137. https://doi.org/10.1016/S0191-8141(98)00046-7

Passchier CW, Trouw RAJ (2005) Microtectonics. Springer, Berlin. https://doi.org/10.1007/3-540-29359-0

Paton C, Hellstrom J, Paul B, Woodhead J, Hergt J (2011) Iolite: Freeware for the visualisation and processing of mass spectrometric data. J Anal Atom Spectr 26(12):2508–2518. https://doi.org/10.1039/c1ja10172b

Petroccia A (2023) Spatial variation of pure and simple shear across transpressive shear zones: flow kinematics map of the

Posada-Asinara shear zone (NE Sardinia, Italy). Rendiconti Online Della Società Geologica Italiana 60:24–36

Petroccia A, Carosi R, Montomoli C, Iaccarino S, Vitale Brovarone A (2022a) Deformation and temperature variation along thrust-sense shear zones in the hinterland-foreland transition zone of collisional settings: a case study from the Barbagia Thrust (Sardinia, Italy). J Struct Geol. https://doi.org/10.1016/j.jsg.2022.104640

Petroccia A, Montomoli C, Iaccarino S, Carosi R (2022b) Geology of the contact area between the Internal and External Nappe Zone of the Sardinian Variscan Belt (Italy): new insights on the complex polyphase deformation occurring in the hinterland-foreland transition zone of collisional belts. J Maps. https://doi.org/10.1080/17445647.2022.2093660

Petroccia A, Carosi R, Montomoli C, Iaccarino S, Vitale Brovarone A (2022c) Thermal variation across collisional orogens: insights from the hinterland-foreland transition zone of the Sardinian Variscan belt. Terra Nova. https://doi.org/10.1111/ter.12635

Platt JP, Vissers RLM (1980) Extensional structures in anisotropic rocks. J Struct Geol 2(4):397–410. https://doi.org/10.1016/0191-8141(80)90002-4

Platt JP, Behr WM, Cooper FJ (2015) Metamorphic core complexes: Windows into the mechanics and rheology of the crust. J Geol Soc Lond 172(1):9–27. https://doi.org/10.1144/jgs2014-036

Rieder M, Cavazzini G, D'yakonov Y, Frank-Kamenetskii V, Gottardi G, Guggenheim S, Koval PV, Müller G, Neiva AMR, Radoslovich EW, Robert JL, Sassi FP, Takeda H, Weiss Z, Wones D (1999) Nomenclature of the micas. Mineral Mag 63(2):267–279. https://doi.org/10.1180/minmag.1999.063.2.13

Robin PYF, Cruden AR (1994) Strain and vorticity patterns in ideally ductile transpression zones. J Struct Geol 16(4):447–466. https://doi.org/10.1016/0191-8141(94)90090-6

Rosenberg CL, Handy MR (2005) Experimental deformation of partially melted granite revisited: implications for the continental crust. J Metamorph Geol 23(1):19–28. https://doi.org/10.1111/j.1525-1314.2005.00555.x

Sanderson DJ, Marchini WRD (1984) Transpression. J Struct Geol 6(5):449–458. https://doi.org/10.1016/0191-8141(84)90058-0

Schulmann K, Thompson AB, Lexa O, Ježek J (2003) Strain distribution and fabric development modeled in active and ancient transpressive zones. Solid Earth 108(B1):ETG-6. https://doi.org/10.1029/2001JB000632

Schulmann K, Edel JB, Martínez Catalán JR, Mazur S, Guy A, Lardeaux JM, Ayarza P, Palomeras I (2022) Tectonic evolution and global crustal architecture of the European Variscan belt constrained by geophysical data. Earth Sci Rev. https://doi.org/10.1016/j.earscirev.2022.104195

Searle MP, Lamont TN (2020) Compressional metamorphic core complexes, low-angle normal faults and extensional fabrics in compressional tectonic settings. Geol Mag 157(1):101–118. https://doi.org/10.1017/S0016756819000207

Simonetti M (2021) The East Variscan Shear Zone: a structural and geochronological review for improving paleogeographic reconstruction of the southern Variscides. Rendiconti Online Della Società Geologica Italiana 55:36–52. https://doi.org/10.3301/ROL.2021.13

Simonetti M, Carosi R, Montomoli C, Langone A, D'Addario E, Mammoliti E (2018) Kinematic and geochronological constraints on shear deformation in the Ferriere-Mollières shear zone (Argentera-Mercantour Massif, Western Alps): implications for the evolution of the Southern European Variscan Belt. Int J Earth Sci 107(6):2163–2189. https://doi.org/10.1007/s00531-018-1593-y

Simonetti M, Carosi R, Montomoli C, Corsini M, Petroccia A, Cottle JM, Iaccarino S (2020a) Timing and kinematics of flow in a transpressive dextral shear zone, Maures Massif (Southern France). Int J Earth Sci 109(7):2261–2285. https://doi.org/10.1007/s00531-020-01898-6

Simonetti M, Carosi R, Montomoli C, Cottle JM, Law RD (2020b) Transpressive deformation in the southern european variscan belt: new insights from the aiguilles rouges massif (Western Alps). Tectonics. https://doi.org/10.1029/2020TC006153

Simonetti M, Carosi R, Montomoli C, Law RD, Cottle JM (2021) Unravelling the development of regional-scale shear zones by a multidisciplinary approach: the case study of the Ferriere-Mollières Shear Zone (Argentera Massif, Western Alps). J Struct Geol 149:104399. https://doi.org/10.1016/j.jsg.2021.104399

Spencer JE, Richard SM, Bykerk Kauffman A, Constenius KN, Valencia VA (2022) Structure, chronology, kinematics, and geodynamics of tectonic extension in the greater Cata-lina metamorphic core complex, southeastern Arizona, USA. Geosphere 18(6):1–36. https://doi.org/10.1130/GES02485.1

Stipp M, Stünitz H, Heilbronner R, Schmid SM (2002a) Dynamic recrystallization of quartz: correlation between natural and experimental conditions. Geol Soc Lond Spec Publ 200:171–190. https://doi.org/10.1144/GSL.SP.2001.200.01.11

Stipp M, Stünitz H, Heilbronner R, Schmid SM (2002b) The eastern tonale fault zone: A natural laboratory for crystal plastic deformation of quartz over a temperature range from 250 to 700 °C. J Struct Geol 24:1861–1884. https://doi.org/10.1016/S0191-8141(02)00035-4

Stüwe K, Powell R (1995) PT paths from modal proportions: application to the Koralm Complex, Eastern Alps. Contrib Mineral Petrol 119(1):83–93. https://doi.org/10.1007/BF00310719

Sullivan WA, Law RD (2007) Deformation path partitioning within the transpressional White Mountain shear zone, California and Nevada. J Struct Geol 29(4):583–599. https://doi.org/10.1016/j.jsg.2006.11.001

Tikoff B, Fossen H (1995) The limitations of three-dimensional kinematic vorticity analysis. J Struct Geol 17(12):1771–1784. https://doi.org/10.1016/0191-8141(95)00069-P

Vanardois J, Roger F, Trap P, Goncalves P, Lanari P, Paquette JL, Marquer D, Cagnard F, Le Bayon B, Barou F (2022a) Exhumation of deep continental crust in a transpressive regime: the example of Variscan eclogites from the Aiguilles-Rouges massif (Western Alps). J Metamorph Geol. https://doi.org/10.1111/jmg.12659

Vanardois J, Trap P, Roger F, Melleton J, Marquer D, Paquette JL, Gonclaves P, Cagnard F, Le Bayon B (2022b) Deformation, crustal melting and magmatism in the crustal-scale East-Variscan Shear Zone (Aiguilles-Rouges and Mont-Blanc massifs, Western Alps). J Struct Geol 163:104724. https://doi.org/10.1016/j.jsg.2022.104724

Vanderhaeghe O, Teyssier (2001) Partial melting and flow of orogens. Tectonophysics 342:451–472. https://doi.org/10.1016/S0040-1951(01)00175-5

Vanderhaeghe O, Oscar L, Gardien V, Moyen JF, Gébelin A, Chelle-Michou C, Couzinié S, Villaros A, Bellanger M (2020) Flow of partially molten crust controlling construction, growth and collapse of the Variscan orogenic belt: the geologic record of the French Massif Central. Bulletin De La Société Géologique De France 191:25. https://doi.org/10.1051/bsgf/2020013

Vollmer FW (2015) EllipseFit 3.2. https://www.frederickvollmer.com/ellipsefit/

Wallis SR, Platt JP, Knott SD (1993) Recognition of synconvergence extension in accretionary wedges with examples from the Caiabrian Arc and the Eastern Alps. Am J Sci 293:463–495. https://doi.org/10.2475/ajs.293.5.463

Warr LN (2021) IMA–CNMNC approved mineral symbols. Mineral Mag 85:291–320. https://doi.org/10.1180/mgm.2021.43

White RW, Powell R, Holland TJB, Johnson TE, Green ECR (2014) New mineral activity–composition relations for thermodynamic

calculations in metapelitic systems. J Metamorph Geol 32(3):261–286. https://doi.org/10.1111/jmg.12071
Whitney DL, Teyssier C, Vanderhaeghe O (2004) Gneiss domes and crustalflow. Gneiss domes in orogeny. Geol S Am S 380:15–33. https://doi.org/10.1130/0-8137-2380-9.15
Whitney DL, Teyssier C, Rey P, Buck WR (2013) Continental and oceanic core complexes. GSA Bull 125(3–4):273–298. https://doi.org/10.1130/B30754.1
Xypolias P (2010) Vorticity analysis in shear zones: a review of methods and applications. J Struct Geol 32:2072–2092. https://doi.org/10.1016/j.jsg.2010.08.009
Zhang B, Chai Z, Yin CY, Huang WT, Wang Y, Zhang JJ, Wang X, Cao K (2017) Intra-continental transpression and gneiss doming in an obliquely convergent regime in SE Asia. J Struct Geol 97:48–70. https://doi.org/10.1016/j.jsg.2017.02.010